



SPE 99743

The Effect of Displacement History on Three-Phase Capillary Pressure and Relative Permeability Derived From Triangular Pore Cross-Sections With Contact-Angle Hysteresis

J.O. Helland, SPE, and S.M. Skjæveland, SPE, University of Stavanger

Copyright 2006, Society of Petroleum Engineers

This paper was prepared for presentation at the 2006 SPE/DOE Symposium on Improved Oil Recovery held in Tulsa, Oklahoma, U.S.A., 22–26 April 2006.

This paper was selected for presentation by an SPE Program Committee following review of information contained in a proposal submitted by the author(s). Contents of the paper, as presented, have not been reviewed by the Society of Petroleum Engineers and are subject to correction by the author(s). The material, as presented, does not necessarily reflect any position of the Society of Petroleum Engineers, its officers, or members. Papers presented at SPE meetings are subject to publication review by Editorial Committees of the Society of Petroleum Engineers. Electronic reproduction, distribution, or storage of any part of this paper for commercial purposes without the written consent of the Society of Petroleum Engineers is prohibited. Permission to reproduce in print is restricted to an abstract of not more than 300 words; illustrations may not be copied. The abstract must contain conspicuous acknowledgment of where and by whom the paper was presented. Write Librarian, SPE, P.O. Box 833836, Richardson, TX 75083-3836, U.S.A., fax 01-972-952-9435.

Abstract

We present a model of mixed-wet triangular tubes that calculates three-phase capillary pressure and relative permeability curves. Several fluid configurations may occur in triangular pore cross-sections, and capillary displacements may either occur as piston-like displacements of the fluids occupied in the bulk, or as piston-like displacements of the fluids in layers. To our knowledge, this latter type of displacement has not been analyzed before in mixed-wet pores. Using minimization of Helmholtz free energy, we derive accurate three-phase capillary entry pressures for such layer displacements, accounting for contact-angle hysteresis. Numerical examples are presented to illustrate how the entry pressures for the different possible displacements relate to each other during gas and water invasion into pores with a specific fluid configuration. It turns out that the entry pressures for related displacements are consistent. This implies that pores occupied by the same fluid in the bulk portion must have the same fluid configuration for a constant value of capillary pressure.

With this model we calculate three-phase capillary pressure and relative permeability, and explore how the saturation-dependencies of these quantities change according to saturation-reversal points. We simulate the sequence of processes primary drainage, imbibition and gas invasion, for different maximum capillary pressures P_{ow}^{\max} after primary drainage. In the simulation results presented here, we find that the oil and gas relative permeability, and their saturation-dependencies, are sensitive to variations of P_{ow}^{\max} , while the water relative permeability is less sensitive. Such effects are absent in cylindrical tubes. This is caused by the capillary entry pressures, which

are strongly affected by hinging interfaces in the corners of angular pores when contact-angle hysteresis is assumed. Thus the choice of pore geometry is important if hysteretic capillary pressure and relative permeability relationships are simulated using network models. With respect to these findings, relative permeability and capillary pressure correlations should be formulated with parameters that strongly depend on saturation-reversal points such that different saturation-dependencies can be accounted for in subsequent invasion processes.

Introduction

Relative permeability and capillary pressure are required as functions of the saturations to solve the equations for three-phase flow in reservoir simulation. These relationships are normally formulated as simple correlations with adjustable parameters. In the reservoir, situations may occur where one of the phases appears or disappears, e.g., during phase transitions between gas and oil, or when a zero residual oil saturation is approached by drainage through continuous spreading layers in the crevices of the pore space. To implement these scenarios in a numerical reservoir simulator without creating convergence problems, the correlations must account for a smooth transition between two- and three-phase flow.

In the oil industry three-phase capillary pressure and relative permeability curves have traditionally been predicted from corresponding two-phase measurements. However, both experimental and numerical work have shown that this practice may not be valid. Moreover, micromodel studies of three-phase flow have revealed that the fluid distribution and the displacement mechanisms at the pore scale may be more complex than for two phases.^{1,2} These findings emphasize the need for direct measurements of three-phase capillary pressure and relative permeability curves for various conditions. However, in three-phase flow there is an infinite number of possible displacement paths because of two independent saturations. Hence, it is impractical to perform time-consuming measurements of a vast amount of different processes for several rock and fluid properties. This points out the importance of developing physically-based pore-scale network models^{3–6} to compute the relative permeability and capillary pressure curves. A pore-scale model, tuned to reproduce the measured data, may be employed to predict these quantities for displacement paths not covered by the measurements.

In a recent paper⁷ we presented a simple bundle-of-triangular-tubes model where the tubes have triangular cross-sections. This is a very simplistic approach for modelling of realistic reservoir rocks. Such a simple model does not incorporate the effect of interconnected pore networks, and hence phase entrapment is absent. However, the angular pore shapes allow for other important physical processes, such as the development of mixed wettability at the pore scale,^{8,9} and drainage through oil layers along the corners.¹⁰ Several fluid configurations can occur in a triangular cross-section, and this requires careful analysis of all possible displacements. Based on the method proposed by van Dijke and Sorbie,¹¹ we derived accurate expressions for the three-phase capillary entry pressures that account for contact-angle hysteresis and the possibility of simultaneous displacement of the fluids occupying the cross-sections. However, piston-like invasion was only assumed to occur as a displacement of fluids occupied in the bulk portion of the pore. More recently, van Dijke *et al.*¹² employed their method to also account for piston-like displacements of fluid layers in the corners of the pores. In the present paper we explain how to calculate entry pressures for such displacements in a model of mixed-wet pores with contact-angle hysteresis.

The developed pore model was employed to simulate three-phase capillary pressure curves for various conditions and to analyze the corresponding saturation-dependencies.⁷ It was found that the reversal point after primary drainage may strongly affect the saturation-dependencies of three-phase capillary pressure in subsequent displacement processes. Experimental measurements have shown that reversal point after primary drainage is related to wettability.¹³ This in turn affects the saturation-dependencies of three-phase capillary pressure and relative permeability.¹⁴⁻¹⁸ In triangular tubes, the maximum capillary pressure after primary drainage, and thereby the reversal point, is related to wettability.¹⁹ Thus, there exists a relationship between the saturation-dependencies and the maximum capillary pressure for triangular tubes.

The present paper represents extensions of the work by Helland and Skjæveland⁷ in two directions: First, we extend the simple pore model to account for layer displacements for mixed-wet conditions and contact-angle hysteresis, following the method by van Dijke *et al.*¹² Second, we extend the model to also account for calculations of three-phase relative permeability. The paper is organized as follows: First we describe a method to calculate advancing and receding contact angles for three phases. Then we briefly describe the main features of the model, before derivations of three-phase entry pressures for bulk and layer displacements are described in detail for cases of gas invasion. Then we present numerical examples to examine how the different entry pressures relate to each other. With the present model we calculate relative permeability and explore if the saturation-dependencies are sensitive to variations of reversal points in the displacement history.

Preliminaries

Wettability and Contact-Angle Hysteresis. The wetting preference of a solid surface in contact with two fluids is typically characterized by the contact angle. Assuming that the denser

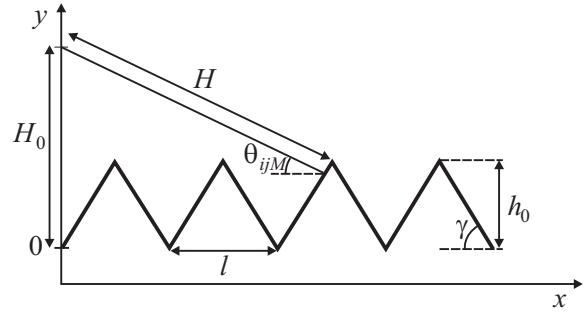


Figure 1: Cross-sectional view of the model for surface roughness along the contact line movement.

phase *j* is wetting relative to phase *i*, then $\cos \theta_{ij} \geq 0$, where the contact angle θ_{ij} is measured through phase *j*. In equilibrium, the horizontal force balance at the fluid-fluid-solid contact line is given by Young's equation:²⁰

$$\sigma_{is} = \sigma_{js} + \sigma_{ij} \cos \theta_{ij}, \dots \dots \dots (1)$$

On smooth solid surfaces the contact angle is uniquely determined by Eq. 1, i.e., $\theta_{ij} = \theta_{ije}$, where θ_{ije} is the intrinsic contact angle. For gas-oil, oil-water and gas-water interfaces located on solid surface, Young's equation provides force balances of all three fluids-fluid-solid contact lines. Elimination of the fluid-solid interfacial tensions then results in a relationship between the three contact angles and the fluid-fluid interfacial tensions:^{21,22}

$$\sigma_{gw} \cos \theta_{gw} = \sigma_{ow} \cos \theta_{ow} + \sigma_{go} \cos \theta_{go}. \dots \dots \dots (2)$$

This equation also emerges from the relation between capillary entry pressures in cylindrical tubes¹⁵ and from analysis of true three-phase systems where gas-oil-water contact lines exist.²³

The contact angle varies with the direction of the contact-line displacement on non-ideal surfaces.²⁴ For example, if oil displaces water, the oil-water interface is receding with the smallest contact angle θ_{owr} , and if water displaces oil, the interface is advancing with the largest contact angle θ_{owa} . The difference between receding and advancing contact angles is referred to as contact angle hysteresis. For intermediate contact-angle values the contact line may be pinned while the contact angle varies between its receding and advancing value. For later use we denote this varying contact angle as the *hinging* contact angle, θ_{ijh} , which satisfies $\theta_{ijr} \leq \theta_{ijh} \leq \theta_{ija}$. Obviously, when contact angle hysteresis is present, the contact angle is not uniquely determined by Eq. 1. The degree of contact angle hysteresis is affected by surface roughness,²⁵ microscopic wettability heterogeneity,²⁶ as well as fluid composition and adsorption of crude oil components.^{27,28} Experimentally measured oil-water receding and advancing contact angles often seem to differ by more than 60°, including cases where $\cos \theta_{owr} > 0$ while $\cos \theta_{owa} < 0$.^{26,28,29} This indicates oil-wet behaviour during waterflooding and water-wet behaviour during oil invasion.

In this work we attribute surface roughness as the source to contact angle hysteresis. To calculate advancing and receding contact angles, we follow the method described by Long *et*

al.²⁴ They calculated contact angle hysteresis on rough and/or heterogeneous surfaces using minimization of surface free energy for a virtual displacement of the contact line. This method requires the geometry of the surface roughness to be specified. We assume an idealized regular model for the surface roughness, where each bump has the shape of an isosceles triangle, characterized by the angle γ between the sides and the baseline. Each bump has the same height h_0 and baseline l , see Fig. 1. This is a 2-dimensional model, and thus all parameters only change in the (x, y) plane. To calculate the free energy change for a virtual displacement of the contact line of a 2-dimensional drop resting on the rough surface shown in Fig. 1, it is assumed that the fluid front is linear in the vicinity of the contact line, that changes in volume are negligible, and that Young's equation is locally valid for the intrinsic contact angle, i.e., with $\theta_{ij} = \theta_{ije}$.

For a displacement x of the fluid front from the initial state to another, the total change in surface free energy for the system is due to changes in solid-fluid areas and fluid-fluid areas:

$$\Delta F_{\text{tot}} = L(\sigma_{js} - \sigma_{is})s(x) + L\sigma_{ij}\Delta H, \dots \dots \dots (3)$$

where L is the front width, s represents the topographic distance along the rough surface, which is related to the displacement in the x -direction through

$$s(x) = \frac{x}{\cos \gamma} \dots \dots \dots (4)$$

The change in linear fluid-front length ΔH is given by

$$\Delta H = H - H_0 = \sqrt{(H_0 - y)^2 + (x)^2} - H_0 \dots \dots (5)$$

Substitution of Eqs. 1, 4, 5 into Eq. 3 then yields²⁴

$$\Delta F = -L\sigma_{ij} \frac{\cos \theta_{ije}}{\cos \gamma} + L\sigma_{ij} \left(\sqrt{(H_0 - y)^2 + x^2} - H_0 \right) \dots (6)$$

The macroscopic apparent contact angle θ_{ijM} is related to the change in free energy through the geometric relation

$$\tan \theta_{ijM} = \frac{H_0 - y}{x} \dots \dots \dots (7)$$

Fig. 2 shows ΔF plotted as a function of θ_{ijM} with $\theta_{ije} = 80^\circ$, $l = 1e-8$ m, $L = 1$ m, $H_0 = 1e-7$ m and $\sigma_{ij} = 0.020$ N/m. The smooth curve was obtained with $\gamma = 0^\circ$, representing a smooth solid surface. In this case there is only one minimum of the surface free energy, which corresponds to the only stable contact angle, $\theta_{ijM} = \theta_{ije}$. The other curve was obtained with $\gamma = 50^\circ$, and in this case several minima of the surface free energy is obtained. The largest and smallest macroscopic contact angles that corresponds to a metastable state is equal to the advancing and receding contact angle, respectively. These contact angles are related to the roughness as follows:

$$\theta_{ija} = \theta_{ije} + \gamma, \dots \dots \dots (8a)$$

$$\theta_{ijr} = \theta_{ije} - \gamma, \dots \dots \dots (8b)$$

In the case of surface roughness, the global minimum corresponds to the so-called system equilibrium contact angle, which

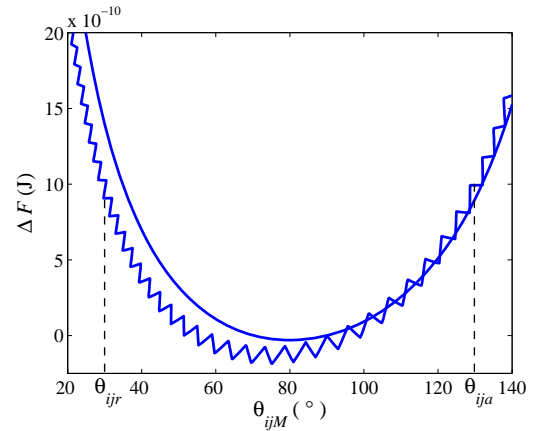


Figure 2: Change of surface free energy plotted as a function of macroscopic contact angle with $\theta_{ije} = 80^\circ$. The smooth curve corresponds to a smooth solid surface ($\gamma = 0^\circ$), and the other curve corresponds to a rough surface ($\gamma = 50^\circ$).

generally differs from the intrinsic contact angle.²⁴ Eq. 8 may be obtained by minimizing the change in surface free energy, $d(\Delta F)/dx = 0$. This yields

$$\frac{\cos \theta_{ije}}{\cos \gamma} - \sin \theta_{ijM} \frac{dy}{dx} + \cos \theta_{ijM} = 0, \dots \dots \dots (9)$$

where $dy/dx = \pm \tan \gamma$. Eq. 9 is solved for θ_{ijM} , and the solutions given by Eq. 8 are obtained.

In the present work we allow for hysteresis in gas-oil, oil-water and gas-water contact angles. If gas displaces oil and water, the gas-oil and gas-water interfaces are receding with contact angles θ_{gor} and θ_{gwr} , respectively. Correspondingly, oil and water displace gas with advancing contact angles θ_{goa} and θ_{gwa} . We first specify intrinsic contact angles that satisfy Eq. 2. Then we calculate advancing and receding contact angles by Eq. 8, assuming a specified γ . In cases where $\theta_{ije} < \gamma$ or $\theta_{ije} > \pi - \gamma$, no global minima of ΔF exist. We interpret this as cases of complete wetting and set $\theta_{ijr} = 0^\circ$ or $\theta_{ija} = 180^\circ$, respectively.

AMs, MTMs and the MS-P method. An important feature of the capillary behaviour in an angular tube is the possibility of simultaneous occupancy of more than one fluid in the cross-section: The wetting phase may reside in the corners after the non-wetting phase has occupied the bulk portion of the pore. A method to calculate capillary entry pressures for piston-like invasion into angular tubes has been developed by Mayer and Stowe,³⁰ who considered breakthrough pressure in the space between packed spheres, and Princen,³¹⁻³³ who considered the height of capillary rise in the space formed between cylinders. The method was referred to as the MS-P method by Mason and Morrow,³⁴ and has later been extended to account for irregular pore shapes^{4,34,35} and mixed-wet conditions.^{4,19} This method is founded on an energy balance equation which equates the virtual work with the associated change of surface free energy

for a small displacement of the interface in the direction along the tube. The energy balance equation then relates the entry radius of curvature to the cross-sectional area exposed to change of fluid occupancy, the bounding cross-sectional fluid-solid and fluid-fluid lengths, and the contact angle.

The analysis for an equilateral triangular pore cross-section is largely simplified as all corners have the same half-angle α and hence the same fluid configuration. There are two scenarios that need to be considered separately depending on the contact angle. As an example, consider invasion of phase i into a uniformly wetted tube initially filled with the denser phase j . If

$$\theta_{ij} < \frac{\pi}{2} - \alpha, \dots \dots \dots (10)$$

phase i occupies the bulk area while phase j is still residing in the corners. If the contact angle does not satisfy Eq. 10, phase i occupies the entire cross-section during invasion. The invading interface separating the bulk fluids is referred to as the main terminal meniscus (MTM), and the interface separating bulk fluid from corner fluid, if present, is referred to as the arc meniscus (AM). The curvature of an AM is represented by a cross-sectional circular arc of radius r_{ij} . Thus, by Laplace's equation, the capillary pressure may be expressed as

$$P_{ij} = P_i - P_j = \frac{\sigma_{ij}}{r_{ij}}. \dots \dots \dots (11)$$

In a system of gas, oil and water, the intermediate wetting phase may be present as layers bounded by the wetting phase in the corners and the non-wetting phase in the bulk of the pore. By definition, the three capillary pressures are related to each other by

$$P_{gw} = P_{go} + P_{ow}. \dots \dots \dots (12)$$

The application of Eq. 11 on all capillary pressures then yields a useful relation between the radii of curvatures of the gas-water, oil-water and gas-oil AMs:

$$\frac{\sigma_{gw}}{r_{gw}} = \frac{\sigma_{go}}{r_{go}} + \frac{\sigma_{ow}}{r_{ow}}. \dots \dots \dots (13)$$

Pore model

The pore network is represented as a bundle of equilateral, triangular, pore cross-sections. The pore size is characterized by the radius of the inscribed circle R . The cross-sectional area of a tube, A , is related to R by

$$A = \frac{3R^2}{\tan \alpha}. \dots \dots \dots (14)$$

The model is programmed to simulate gas, oil and water invasion processes in any sequence starting with primary drainage of a waterfilled and water-wet medium. An invasion process is simulated by increasing or decreasing a capillary pressure stepwise until some maximum or minimum value is reached. For each step the cross-sectional fluid occupancies in the tubes are updated based on a comparison with the capillary entry pressure associated with the favourable displacement. The saturations are calculated based on the fraction of the cross-sectional area that each phase occupies.

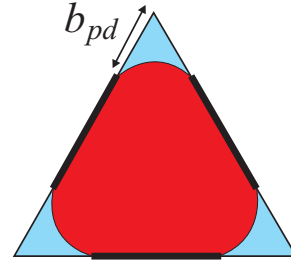


Figure 3: Final configuration of a tube after primary drainage. The bold lines along the sides represent the lengths of the pore wall where the wettability may have changed. The distances b_{pd} in the corners remain water-wet.

Primary Drainage and Wettability Alteration. Initially all tubes are water-filled and strongly water-wet, and hence the contact angle during primary drainage, θ_{pd} , is always small and satisfies Eq. 10. To establish pores of mixed wettability after primary drainage, we adopt the model proposed by Kovscek *et al.*⁸ However, we do not consider stability and collapse of thin water films along the sides of the pore walls as this requires knowledge of the disjoining pressure isotherm and molecular properties. Instead, we assume that oil always contacts the pore walls of the invaded tubes, and hence the sides may experience a wettability alteration while the corners remain water-wet. The final configuration of a tube after primary drainage is shown in **Fig. 3**. The distance b_{pd} of the solid surface that remains water-wet is given by

$$b_{pd} = \frac{\sigma_{ow} \cos(\theta_{pd} + \alpha)}{P_{ow}^{max} \sin \alpha}, \dots \dots \dots (15)$$

where P_{ow}^{max} is the capillary pressure at the end of primary drainage.

For subsequent invasion processes, receding and advancing contact angles are calculated on the surface of potentially altered wettability as explained in the previous section. To model cases where wettability alteration does not occur, we specify contact angles that represent water-wet conditions.

Fluid Configurations. Contact angle hysteresis leads to a diversity of possible fluid configurations that can occur in simulations of different sequences of the invasion processes. The number of configurations are restricted by the following assumptions: We always consider cases where oil is wetting relative to gas, i.e., $\theta_{gor} \leq \pi/2$ and $\theta_{goa} \leq \pi/2$. A maximum number of two AMs are allowed to be present on the surface exposed to a potential wettability change. An additional AM may be located at position b_{pd} . Finally, we do not study situations where the gas pressure is large enough for gas invasion into tubes and corners where oil has never been. We refer to Helland and Skjæveland⁷ for a discussion of the consequences of these assumptions. **Fig. 4** shows all the configurations that are allowed based on the above constraints. Configuration A illustrates a tube that has always been water-filled and water-wet. The configurations B–Q represent tubes that at some point have been invaded by oil and thus may have altered wettability.

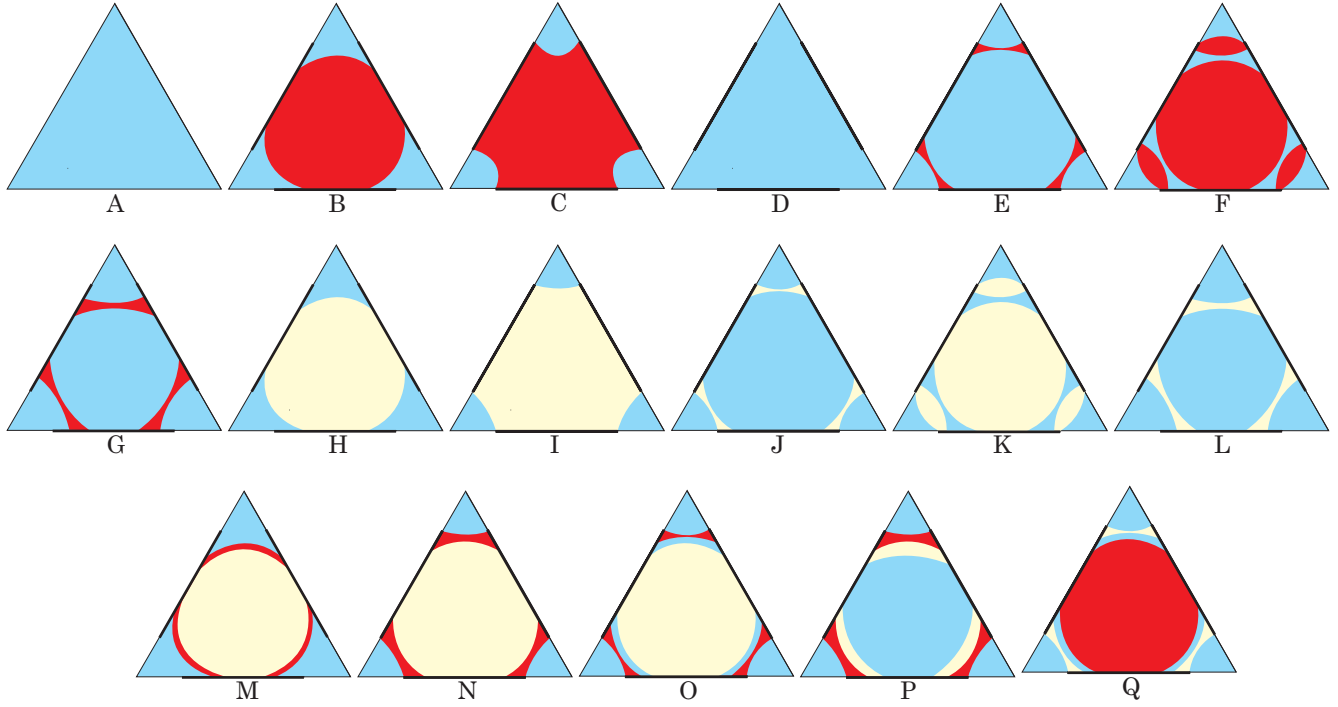


Figure 4: Fluid configurations for any sequences of the invasion processes, with water in blue, oil in red, and gas in yellow. The bold lines along the sides represent the lengths with potentially altered wettability. Oil is always assumed to be wetting relative to gas.

The curvatures of the gas-oil interfaces present in the configurations are always positive, whereas the gas-water and oil-water interfaces may have positive or negative curvatures to satisfy Eq. 13. Three-phase fluid configurations in mixed-wet angular tubes have previously been analyzed by Piri and Blunt.^{6,36,37} As opposed to us, they also consider cases where gas is wetting relative to oil. Gas-water and oil-water AMs located at position b_{pd} may hinge with contact angles varying with the capillary pressures. Oil-water AMs located at this position are also allowed to move on to the water-wet surface when the hinging contact angle has reached θ_{pd} . This happens when $P_{ow} = P_{ow}^{\max}$, and a further increase of P_{ow} causes the length of the water-wet surface, b_{pd} , to decrease additionally. The AMs located on the surface of altered wettability may also hinge at fixed positions while the contact angles change with capillary pressure. The contact angles hinge according to

$$\theta_{ijh} = \begin{cases} \arccos\left(\frac{P_{ij}b_{ij}\sin\alpha}{\sigma_{ij}}\right) - \alpha & \text{if bulk phase } i \text{ is} \\ & \text{bounded by} \\ & \text{corner phase } j, \\ \arccos\left(\frac{P_{ij}b_{ij}\sin\alpha}{\sigma_{ij}}\right) + \alpha & \text{if bulk phase } j \text{ is} \\ & \text{bounded by} \\ & \text{corner phase } i, \end{cases} \quad (16)$$

where $ij = go, ow, gw$, and b_{ij} is the distance from the apex of

the corner to the contact line. If the advancing or receding contact angle is reached, the AMs begin to move at constant contact angles during a further change of capillary pressure. The position b_{ij} is then changing according to

$$b_{ij} = \begin{cases} \frac{\sigma_{ij}\cos(\theta_{ij} + \alpha)}{P_{ij}\sin\alpha} & \text{if bulk phase } i \text{ is bounded} \\ & \text{by corner phase } j, \\ \frac{\sigma_{ij}\cos(\theta_{ij} - \alpha)}{P_{ij}\sin\alpha} & \text{if bulk phase } j \text{ is bounded} \\ & \text{by corner phase } i, \end{cases} \quad (17)$$

where θ_{ij} is equal to θ_{ijr} or θ_{ija} depending on the direction of the displacement.

Three-phase capillary entry pressures

The actual displacement occurring when the invading fluid enters a pore with any of the cross-sectional fluid configurations shown in **Fig. 4** depends on the combinations of the contact angles and the capillary pressures. We calculate three-phase capillary entry pressures using the method proposed by van Dijke and Sorbie.¹¹ They extended the MS-P method to also account for three phases. Capillary entry pressures were calculated from an energy balance equation which equates the virtual work with the corresponding change in surface free energy for a small displacement of the MTM in the direction along the tube. The

energy balance then relates the entry radii of curvatures to the geometry of the cross-sectional fluid configurations, accounting for the possibility of simultaneous displacement of the fluids occupying the pore. In such three-phase situations, the capillary entry pressure for the displacement of the interface separating the two bulk fluids (i.e., the MTM) also depends on the pressure in the remaining fluid present in the corners. In cases where only some of the bulk fluid is displaced, the method degenerates to the well-known MS–P method. Van Dijke *et al.*¹² have also applied the energy balance to derive expressions for piston-like invasion of fluid layers in the corners of angular pores. It turns out that the resulting entry pressures are favourable compared to the commonly assumed geometric conditions for fluid-layer existence.

The method to calculate three-phase entry pressures has recently been extended by Helland and Skjæveland⁷ and Piri and Blunt³⁷ to also account for mixed wettability and contact-angle hysteresis following the approach by Ma *et al.*¹⁹ for two phases. Thus, the effect of hinging AMs stuck at fixed positions along the pore walls were incorporated in the derivations. Contact-angle hysteresis leads to several possible combinations of the three-phase contact angles and an increased number of possible fluid configurations, as compared to the case of uniform wettability. This also leads to several possible piston-like displacements if contact-angle hysteresis is present. Helland and Skjæveland⁷ analyzed gas invasion into the bulk of configuration E, which may result in a direct displacement to configuration I, N or O. However, in this work piston-like displacement of fluid layers were not considered. In the following we extend this work to also account for fluid layer displacements for mixed-wet conditions and contact-angle hysteresis. Based on the approach by¹² we calculate capillary entry pressures for layer displacements that can occur in mixed-wet pores where multiple fluid layers may be present. We analyze both bulk and layer displacements for cases of gas and water invasion. As the illustrating example, we consider gas into configuration E, as this configuration can occur for a wide range of contact angles and thus the different aspects of our approach can be elucidated. First we revisit necessary conditions for layer existence, define notation and parameters employed in the derivations, and formulate the general energy balance equations from which the entry pressures for any displacement between the different fluid configurations presented in **Fig. 4** are derived.

Geometric Conditions for Layer Existence. The conditions for layer formation are required to determine the correct displacement in each case. The basic necessary condition is that formation of additional AMs in the corners must be geometrically possible based on the values of the contact angles. A new AM separating phase *i* from phase *j* at a position $b_{ij} > b_{pd}$ can only form if the contact angle satisfy the following condition:

$$\begin{aligned} \theta_{ij} < \frac{\pi}{2} - \alpha & \text{ if invading phase } i \text{ is bounded} \\ & \text{by corner phase } j, \\ \theta_{ij} > \frac{\pi}{2} + \alpha & \text{ if invading phase } j \text{ is bounded} \\ & \text{by corner phase } i, \end{aligned} \quad \dots \quad (18)$$

where $ij = go, ow, gw$, and θ_{ij} is equal to θ_{ijr} or θ_{ija} depending on the direction of the displacement. However, if Eq. 18 is not satisfied, a new AM still forms at position $b_{ij} = b_{pd}$ since then the AM is assumed to hinge with contact angle θ_{ijh} . A second condition required for layer existence is that the capillary entry pressure associated with the layer-forming displacement must be favourable compared to the critical capillary pressure calculated when the AMs surrounding the layer meet.^{11,12} This geometrically limiting capillary pressure corresponds to a configuration where the AMs either meet at their midpoints or when the contact lines coincide, depending on the combinations of the contact angles.^{38,39}

Notation and Definitions. To formulate general energy balance equations from which capillary entry pressures for piston-like layer and bulk displacements between the configurations shown in **Fig. 4** can be calculated, we first have to introduce some notation. AMs formed by the same pair of phases in a corner are numbered in order from the corner towards the center of the cross-section. The *k*th AM between phases *i* and *j* is referred to as *ij* AM *k*. We apply the indicator notation¹²

$$I_{ij}^{(k)} = \begin{cases} 1 & \text{if } ij \text{ AM } k \text{ bounds bulk phase } i \\ & \text{and corner phase } j, \\ -1 & \text{if } ij \text{ AM } k \text{ bounds bulk phase } j \\ & \text{and corner phase } i, \\ 0 & \text{otherwise,} \end{cases} \quad \dots \quad (19)$$

where $ij = go, ow, gw$. Furthermore, the total number of *ij* AMs present in a corner before displacement is denoted N_{ij}^{init} , while the total number of *ij* AMs in the corner after displacement is denoted N_{ij}^{fin} . The cross-sectional *bulk* area bounded by *ij* AM *k* is denoted $A_{ij}^{(k)}$. The bounding solid-fluid and fluid-fluid lengths are denoted $L_{sij}^{(k)}$ and $L_{fij}^{(k)}$, respectively. With reference to **Fig. 5**, these parameters are defined as follows:

$$A_{ij}^{(k)} = \frac{R^2}{2 \tan \alpha} - \frac{r_{ij}^2}{2 \sin \alpha} h_{ij}^{(k)} \quad \dots \quad (20)$$

where

$$h_{ij}^{(k)} = \begin{cases} \sin \beta_{ij}^{(k)} \cos \theta_{ij}^{(k)} - \beta_{ij}^{(k)} \sin \alpha & \text{if } I_{ij}^{(k)} = 1, \\ \sin \beta_{ij}^{(k)} \cos \theta_{ij}^{(k)} + \beta_{ij}^{(k)} \sin \alpha & \text{if } I_{ij}^{(k)} = -1, \end{cases} \quad (21)$$

$$L_{fij}^{(k)} = r_{ij} \beta_{ij}^{(k)}, \quad \dots \quad (22)$$

and

$$L_{sij}^{(k)} = \frac{R}{\tan \alpha} - b_{ij}^{(k)}, \quad \dots \quad (23)$$

where

$$b_{ij}^{(k)} = \frac{r_{ij} \sin \beta_{ij}^{(k)}}{\sin \alpha}, \quad \dots \quad (24)$$

and

$$\beta_{ij}^{(k)} = \begin{cases} \frac{\pi}{2} - \alpha - \theta_{ij}^{(k)} & \text{if } I_{ij}^{(k)} = 1, \\ \frac{\pi}{2} + \alpha - \theta_{ij}^{(k)} & \text{if } I_{ij}^{(k)} = -1. \end{cases} \quad \dots \quad (25)$$

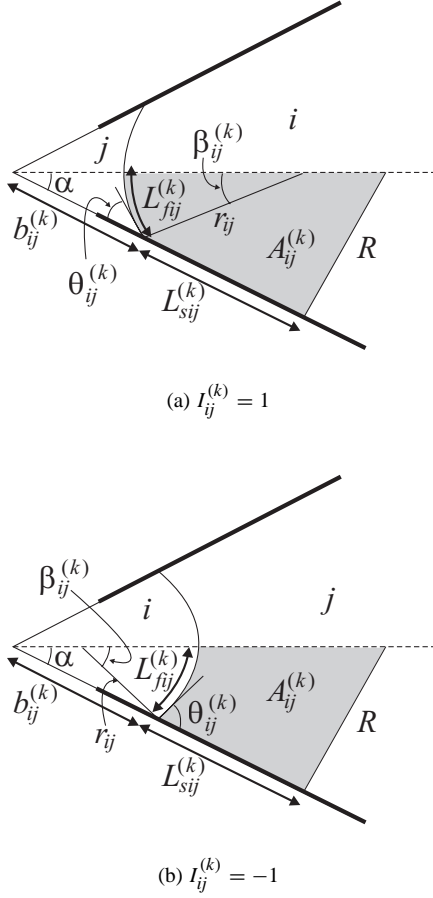


Figure 5: Representation of the cross-sectional parameters of ij AM k .

Eqs. (20)–(25) are written with general contact angles $\theta_{ij}^{(k)}$ that may be equal to $\theta_{ijh}^{(k)}$, θ_{ijr} or θ_{ija} . We also employ the notation $\beta_{ijr} = \beta_{ij}^{(k)}(\theta_{ijr})$, $\beta_{ija} = \beta_{ij}^{(k)}(\theta_{ija})$ and $\beta_{ijh} = \beta_{ij}^{(k)}(\theta_{ijh})$. Similarly, we denote $h_{ijr} = h_{ij}^{(k)}(\theta_{ijr})$, $h_{ija} = h_{ij}^{(k)}(\theta_{ija})$.

Energy Balance Equations.

Gas Invasion. With the above notation, we find that the virtual external work required for gas invasion into the configurations presented in **Fig. 4** may be written in generalized form as

$$W = \{P_{cgw}(\sum_{k=1}^{N_{gw}^{fin}} A_{gw}^{(k)} I_{gw}^{(k)} - \sum_{k=1}^{N_{gw}^{init}} A_{gw}^{(k)} I_{gw}^{(k)}) + P_{cgo}(\sum_{k=1}^{N_{go}^{fin}} A_{go}^{(k)} I_{go}^{(k)} - \sum_{k=1}^{N_{go}^{init}} A_{go}^{(k)} I_{go}^{(k)}) + (P_{cgw} - P_{cgo}) \times (\sum_{k=1}^{N_{ow}^{fin}} A_{ow}^{(k)} I_{ow}^{(k)} - \sum_{k=1}^{N_{ow}^{init}} A_{ow}^{(k)} I_{ow}^{(k)})\} dx. \quad (26)$$

The corresponding change in surface free energy may be written in generalized form as

$$dF = \{\sigma_{gw} \cos \theta_{gwr} (\sum_{k=1}^{N_{gw}^{fin}} L_{sgw}^{(k)} I_{gw}^{(k)} - \sum_{k=1}^{N_{gw}^{init}} L_{sgw}^{(k)} I_{gw}^{(k)}) + \sigma_{gw} (\sum_{k=1}^{N_{gw}^{fin}} L_{fgw}^{(k)} - \sum_{k=1}^{N_{gw}^{init}} L_{fgw}^{(k)}) + \sigma_{go} \cos \theta_{gor} (\sum_{k=1}^{N_{go}^{fin}} L_{sgo}^{(k)} I_{go}^{(k)} - \sum_{k=1}^{N_{go}^{init}} L_{sgo}^{(k)} I_{go}^{(k)}) + \sigma_{go} (\sum_{k=1}^{N_{go}^{fin}} L_{fgo}^{(k)} - \sum_{k=1}^{N_{go}^{init}} L_{fgo}^{(k)}) + (\sigma_{gw} \cos \theta_{gwr} - \sigma_{go} \cos \theta_{gor}) \times (\sum_{k=1}^{N_{ow}^{fin}} L_{sow}^{(k)} I_{ow}^{(k)} - \sum_{k=1}^{N_{ow}^{init}} L_{sow}^{(k)} I_{ow}^{(k)}) + \sigma_{ow} (\sum_{k=1}^{N_{ow}^{fin}} L_{fow}^{(k)} - \sum_{k=1}^{N_{ow}^{init}} L_{fow}^{(k)})\} dx. \quad (27)$$

The energy balance equation, $W = dF$ is solved to obtain the capillary entry pressures P_{cij} for the various displacements that are possible. For later use we denote the entry pressure for a specified displacement from configuration X to Y as $P_{cij}^{X \rightarrow Y}$. For the fluid configurations considered in this work, Eqs. 26, 27 apply with some restrictions: Oil is always wetting relative to gas, and hence $I_{go}^{(k)} \neq -1$. At most three AMs can be present in a single corner at the same time, implying $\sum_{ij=go,ow,gw} N_{ij}^{init} \leq 3$ and $\sum_{ij=go,ow,gw} N_{ij}^{fin} \leq 3$. Moreover, $N_{go}^{init} \leq 1$, and $N_{go}^{fin} \leq 1$, since at most one gas-oil AM is present in a corner.

Water Invasion. The virtual external work required for water invasion into any of the configurations in **Fig. 4** may be written in generalized form as

$$W = \{P_{cgw}(\sum_{k=1}^{N_{gw}^{fin}} A_{gw}^{(k)} I_{gw}^{(k)} - \sum_{k=1}^{N_{gw}^{init}} A_{gw}^{(k)} I_{gw}^{(k)}) + P_{cow}(\sum_{k=1}^{N_{ow}^{fin}} A_{ow}^{(k)} I_{ow}^{(k)} - \sum_{k=1}^{N_{ow}^{init}} A_{ow}^{(k)} I_{ow}^{(k)}) + (P_{cgw} - P_{cow}) \times (\sum_{k=1}^{N_{go}^{fin}} A_{go}^{(k)} I_{go}^{(k)} - \sum_{k=1}^{N_{go}^{init}} A_{go}^{(k)} I_{go}^{(k)})\} dx. \quad (28)$$

The corresponding change in surface free energy is given by

$$dF = \{\sigma_{gw} \cos \theta_{gwa} (\sum_{k=1}^{N_{gw}^{fin}} L_{sgw}^{(k)} I_{gw}^{(k)} - \sum_{k=1}^{N_{gw}^{init}} L_{sgw}^{(k)} I_{gw}^{(k)}) + \sigma_{gw} (\sum_{k=1}^{N_{gw}^{fin}} L_{fgw}^{(k)} - \sum_{k=1}^{N_{gw}^{init}} L_{fgw}^{(k)}) + \sigma_{ow} \cos \theta_{owa} (\sum_{k=1}^{N_{ow}^{fin}} L_{sow}^{(k)} I_{ow}^{(k)} - \sum_{k=1}^{N_{ow}^{init}} L_{sow}^{(k)} I_{ow}^{(k)}) + \sigma_{ow} (\sum_{k=1}^{N_{ow}^{fin}} L_{fow}^{(k)} - \sum_{k=1}^{N_{ow}^{init}} L_{fow}^{(k)}) + (\sigma_{gw} \cos \theta_{gwa} - \sigma_{ow} \cos \theta_{owa}) \times (\sum_{k=1}^{N_{go}^{fin}} L_{sgo}^{(k)} I_{go}^{(k)} - \sum_{k=1}^{N_{go}^{init}} L_{sgo}^{(k)} I_{go}^{(k)}) + \sigma_{go} (\sum_{k=1}^{N_{go}^{fin}} L_{fgo}^{(k)} - \sum_{k=1}^{N_{go}^{init}} L_{fgo}^{(k)})\} dx. \quad (29)$$

Gas into Configuration E. We consider the sequence of processes primary drainage, wettability alteration and gas invasion. Configuration E may then occur when water invades configuration C. In the subsequent gas invasion, P_{ow} is constant, and the

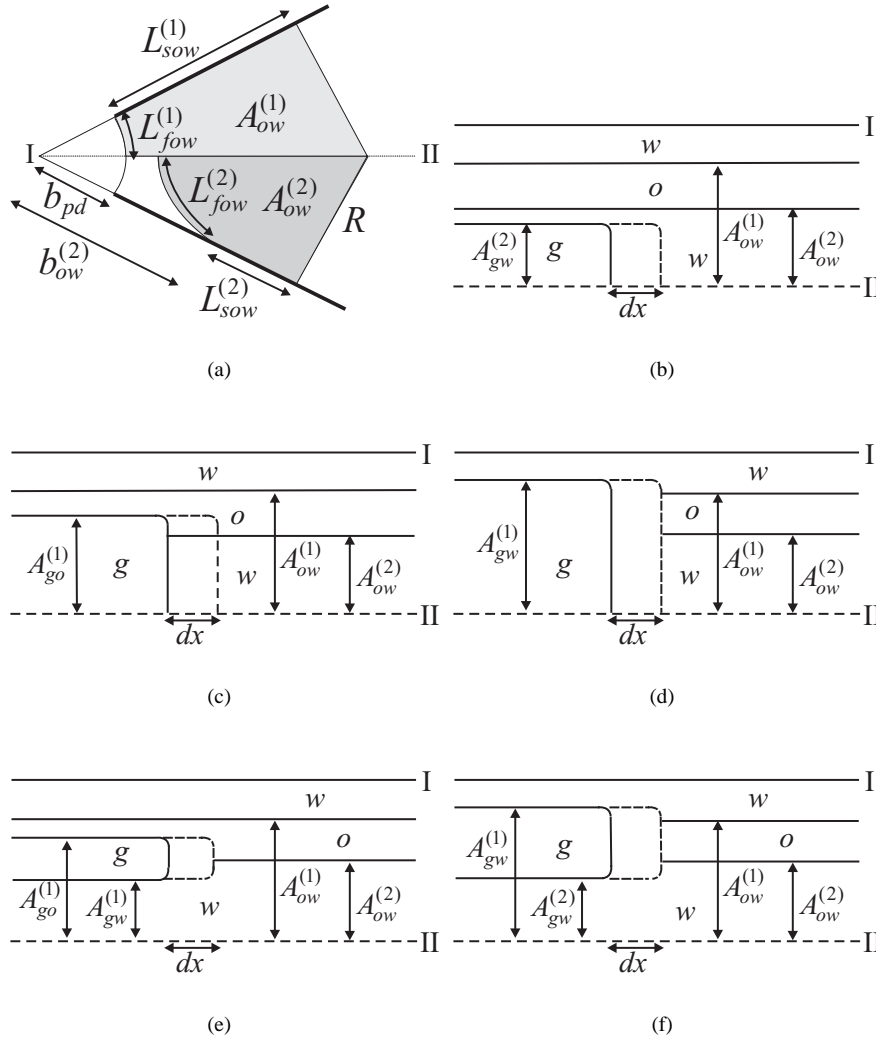


Figure 6: (a) Oil-water parameters for configuration E (Notice that $b_{ow}^{(1)} = b_{pd}$). (b) The displacement E to O. (c) The displacement E to N. (d) The displacement E to P. (e) The displacement E to J.

capillary entry pressures P_{cgo} and P_{cgw} are calculated by solving $W = dF$ obtained from Eqs. 26, 27. Eq. 12 relates P_{ow} , P_{cgo} and P_{cgw} to each other, and hence the energy balance is expressed in terms of only one of the unknown entry pressures. For convenience we prefer to solve this equation for the entry radii of curvatures, and then calculate the corresponding entry pressures using Eq. 11. For configuration E, $N_{gw}^{init} = N_{go}^{init} = 0$ and $N_{ow}^{init} = 2$. The oil-water parameters required for the calculations are known from the end of imbibition, and they are indicated in Fig. 6 (a). Fig. 6 (b)–(d) illustrate all the possible bulk and layer displacements that can occur when gas invades configuration E. We calculate the entry pressures for these displacements and study how they relate to each other for all combinations of the contact angles. The bulk displacements were analyzed elsewhere,⁷ and therefore we emphasize the treatment

of the layer displacements in the following.

$\theta_{gwr} < \pi/2 - \alpha$ and $\theta_{gor} < \pi/2 - \alpha$. For this contact-angle combination the bulk displacements from configuration E to O, N or I are all possible. For the displacement to configuration O, Eqs. 26, 27 apply with $N_{go}^{fin} = 0$, $N_{gw}^{fin} = 1$ and $N_{ow}^{fin} = 2$. This yields

$$\frac{A_{gw}^{(1)}}{r_{gw}} = L_{sgw}^{(1)} \cos \theta_{gwr} + L_{fgw}^{(1)}, \dots \dots \dots (30)$$

where the entry pressure has been eliminated by Eq. 11. This is a simple two-phase displacement without hinging AMs in the corners, and hence $A_{gw}^{(1)}$, $L_{sgw}^{(1)}$ and $L_{fgw}^{(1)}$ appears with $\theta_{gw}^{(1)} = \theta_{gwr}$. The solution of Eq. 30 yields an explicit expression for the entry pressure $P_{cgw}^{E \rightarrow O}$ that can be found elsewhere.¹⁹

To determine if the displacement from configuration E to O is valid, we must require that displacements resulting from gas into configuration O will occur at higher entry pressures. Therefore, we must analyze the piston-like layer displacements from configuration O to N and I. The displacement from configuration O to N is similar to the displacements analyzed by van Dijke *et al.*¹² In this case, $N_{ow}^{init} = 2$, $N_{go}^{init} = 0$, $N_{gw}^{init} = 1$ for configuration O, and $N_{ow}^{fin} = 1$, $N_{go}^{fin} = 1$, $N_{gw}^{fin} = 0$ for configuration N. The energy balance then yields

$$\begin{aligned} & \frac{\sigma_{gw}}{r_{gw}}(A_{ow}^{(2)} - A_{gw}^{(1)}) + \frac{\sigma_{go}}{r_{go}}(A_{go}^{(1)} - A_{ow}^{(2)}) = \\ & \sigma_{gw} \cos \theta_{gwr}(L_{sow}^{(2)} - L_{sgw}^{(1)}) - \sigma_{gw} L_{fgw}^{(1)} + \\ & \sigma_{go} \cos \theta_{gor}(L_{sgo}^{(1)} - L_{sow}^{(2)}) + \sigma_{go} L_{fgo}^{(1)} - \sigma_{ow} L_{fow}^{(2)}, \end{aligned} \quad (31)$$

when the entry pressures are eliminated by Eq. 11. Using Eqs. 20–25 with $\theta_{go}^{(1)} = \theta_{gor}$ and $\theta_{gw}^{(1)} = \theta_{gwr}$, Eq. 32 may be written

$$\begin{aligned} & -\sigma_{ow} \sigma_{go} h_{gor} r_{go}^2 + \{\sigma_{ow}^2 (2 \cos \theta_{ow}^{(2)} \sin \beta_{ow}^{(2)} - h_{ow}^{(2)}) \\ & - 2\sigma_{ow} \sin \beta_{ow}^{(2)} (\sigma_{gw} \cos \theta_{gwr} - \sigma_{go} \cos \theta_{gor}) \\ & + \sigma_{gw}^2 h_{gwr} - \sigma_{go}^2 h_{gor}\} r_{ow} r_{go} \\ & + \{\sigma_{ow} \sigma_{go} (2 \cos \theta_{ow}^{(2)} \sin \beta_{ow}^{(2)} - h_{ow}^{(2)}) \\ & - 2\sigma_{go} \sin \beta_{ow}^{(2)} (\sigma_{gw} \cos \theta_{gwr} - \sigma_{go} \cos \theta_{gor})\} r_{ow}^2 = 0. \end{aligned} \quad (32)$$

Eq. 32 is similar to the equation derived by van Dijke *et al.*¹² The only difference is that we consider contact-angle hysteresis, and hence the contact angles do not necessarily satisfy Eq. 2. It is easy to show that Eq. 32 reduces to the analogous equation of van Dijke *et al.* when the contact angles do satisfy Eq. 2. We solve Eq. 32 for r_{go} and calculate the entry pressure $P_{cgo}^{O \rightarrow N}$ from Eq. 11. The correct solution must satisfy

$$\frac{\sigma_{go} \sin \beta_{gor}}{b_{ow}^{(2)} \sin \alpha} < P_{cgo}^{O \rightarrow N} < P_{go}^{col}, \quad \dots \dots \dots (33)$$

where P_{go}^{col} is the layer-collapse capillary pressure calculated when the two AMs surrounding the water layer in configuration O meet:

$$P_{go}^{col} = \begin{cases} P_{ow} \left(\frac{\sigma_{gw} \cos \theta_{gwr} - \sin \alpha}{\sigma_{ow} \cos \theta_{ow}^{(2)} + \sin \alpha} - 1 \right) & \text{if } \theta_{gwr} < \pi - \theta_{ow}^{(2)}, \\ P_{ow} \left(\frac{\sigma_{gw} \cos(\theta_{gwr} + \alpha)}{\sigma_{ow} \cos(\theta_{ow}^{(2)} - \alpha)} - 1 \right) & \text{if } \theta_{gwr} \geq \pi - \theta_{ow}^{(2)}. \end{cases} \quad (34)$$

Thus, the inequality to the right in Eq. 33 states that the water layer must exist in order for the displacement to occur. The inequality to the left states that the invading gas-oil AM must be located at a position $b_{go}^{(1)} < b_{ow}^{(2)}$. The latter condition only applies if contact-angle hysteresis is assumed. If contact-angle hysteresis is absent, we only require $P_{cgo}^{O \rightarrow N} < P_{go}^{col}$.

If no solution $P_{cgo}^{O \rightarrow N}$ satisfies Eq. 33, we calculate the entry pressure for the displacement again assuming that the invading gas-oil AM hinges with contact angle $\theta_{goh}^{(1)}$ at the fixed position $b_{go}^{(1)} = b_{ow}^{(2)}$. In this case Eq. 31 applies with $L_{sgo}^{(1)} = L_{sow}^{(2)}$. Because of the hinging gas-oil AM, no explicit solution can be derived in this case, and the entry pressures must be calculated by an iterative procedure. We first assume an initial value for the gas-oil entry radius of curvature, e.g., $r_{go} = \sigma_{go} / P_{cgo}^{E \rightarrow O}$, and obtain an initial value r_{gw} from Eq. 13. Using $\theta_{gw}^{(1)} = \theta_{gwr}$, we then calculate $b_{gw}^{(1)}$ from Eq. 24, $A_{gw}^{(1)}$ from Eq. 20, $L_{sgw}^{(1)}$ from Eq. 22 and $L_{fgw}^{(1)}$ from Eq. 23. The gas-oil parameters are calculated correspondingly, except that the angle $\beta_{goh}^{(1)}$ now is obtained from Eq. 24 with the known position $b_{go}^{(1)} = b_{ow}^{(2)}$. The parameters $A_{go}^{(1)}$ and $L_{fgo}^{(1)}$ are then calculated using $\beta_{goh}^{(1)}$. Eventually, a new value for r_{go} is obtained from the energy balance, Eq. 31. This procedure is repeated until a converged value of r_{go} is obtained, and the capillary entry pressure $P_{cgo}^{O \rightarrow N}$ can be calculated from Eq. 11.

Gas invasion into configuration O may also occur in a displacement where both the water and oil layers are displaced simultaneously, resulting in configuration I. The general energy balance, given by Eqs. 26, 27, now applies with $N_{ow}^{fin} = N_{go}^{fin} = 0$ and $N_{gw}^{fin} = 1$ for the final configuration I. Since the gas-water AM in the corner is replaced by a similar gas-water AM at a different position during the displacement, we must specify if the gas-water parameters are calculated before or after the displacement. With this slight change of notation the energy balance yields

$$\begin{aligned} & \frac{\sigma_{gw}}{r_{gw}}(A_{gw}^{(1)}|_{fin} - A_{gw}^{(1)}|_{init}) + \left(\frac{\sigma_{gw}}{r_{gw}} - \frac{\sigma_{go}}{r_{go}} \right) (A_{ow}^{(2)} - A_{ow}^{(1)}) \\ & = \sigma_{gw} \cos \theta_{gwr}(L_{sow}^{(2)} - L_{sgw}^{(1)}|_{init}) + \sigma_{gw}(L_{fgw}^{(1)}|_{fin} - \\ & L_{fgw}^{(1)}|_{init}) + \sigma_{go} \cos \theta_{gor}(L_{sgo}^{(1)} - L_{sow}^{(2)}) - \sigma_{ow}(L_{fow}^{(1)} + L_{fow}^{(2)}), \end{aligned} \quad (35)$$

where $L_{sow}^{(1)} = L_{sgw}^{(1)}|_{fin}$ since the final gas-water AM is assumed to hinge at position $b_{gw}|_{fin} = b_{pd}$. The entry pressure is again calculated numerically. We specify an initial value r_{gw} , e.g., $r_{gw} = \sigma_{gw} / P_{cgw}^{E \rightarrow O}$, and calculate r_{go} from Eq. 13. With $\theta_{gw}^{(1)}|_{init} = \theta_{gwr}$, we calculate $A_{gw}^{(1)}|_{init}$, $L_{fgw}^{(1)}|_{init}$, $L_{sgw}^{(1)}|_{init}$ from Eqs. 20–23. For the final gas-water AM, we first calculate $\beta_{gw}|_{fin}$ from Eq. 24 with $b_{gw}|_{fin} = b_{pd}$, and then we calculate $A_{gw}^{(1)}|_{fin}$, $L_{fgw}^{(1)}|_{fin}$, $L_{sgw}^{(1)}|_{fin}$ from Eqs. 20–23. A new value for r_{gw} is finally obtained from Eq. 35. The procedure is repeated until convergence, and the entry pressure $P_{cgw}^{O \rightarrow I}$ is finally calculated from Eq. 11.

At this stage we have considered the “group” of layer displacements that restricts the existence of configuration O. However, to determine if configuration O can result from gas invasion into configuration E, we must also calculate the entry pressures for the other bulk displacements and their associated restricting layer displacements.

The bulk displacement from configuration E to N is restricted by the layer displacement N to I only. The energy balance for displacement E to N is obtained with $N_{ow}^{fin} = 1$, $N_{go}^{fin} = 1$ and $N_{gw}^{fin} = 0$ in Eqs. 26, 27. This yields

$$\begin{aligned} \frac{\sigma_{gw}}{r_{gw}} A_{gw}^{(2)} + \frac{\sigma_{go}}{r_{go}} (A_{go}^{(1)} - A_{ow}^{(2)}) = \\ \sigma_{gw} \cos \theta_{gwr} L_{sgw}^{(2)} + \sigma_{go} \cos \theta_{gor} (L_{sgo}^{(1)} - L_{sow}^{(2)}) \cdot \cdot \cdot \quad (36) \\ \sigma_{go} L_{fgo}^{(1)} - \sigma_{go} L_{fow}^{(2)}. \end{aligned}$$

The details concerning the entry-pressure calculation for this displacement was described by Helland and Skjæveland.⁷ We only mention that Eq. 36 may be reformulated as a polynomial, and an explicit expression for the entry pressure $P_{cgo}^{E \rightarrow N}$ can be obtained, following the method by van Dijke and Sorbie.¹¹ However, with contact-angle hysteresis, the gas-oil AM may invade at position $b_{go}^{(1)} = b_{ow}^{(2)}$ with a hinging contact angle such that $L_{sgo}^{(2)} = L_{sow}^{(2)}$ in Eq. 36.

The layer displacement N to I must occur at a higher entry pressure if configuration N can form. For this displacement, configuration N yields $N_{ow}^{init} = 1$, $N_{go}^{init} = 0$ and $N_{gw}^{init} = 0$, and the final configuration I yields $N_{ow}^{fin} = N_{go}^{fin} = 0$ and $N_{gw}^{fin} = 1$. The energy balance equation may then be formulated as

$$\begin{aligned} \frac{\sigma_{gw}}{r_{gw}} (A_{gw}^{(1)} - A_{ow}^{(1)}) + \frac{\sigma_{go}}{r_{go}} (A_{ow}^{(1)} - A_{go}^{(1)}) = \\ \sigma_{go} \cos \theta_{gor} (L_{sow}^{(1)} - L_{sgo}^{(1)}) + \sigma_{gw} L_{fgw}^{(1)} - \sigma_{go} L_{fgo}^{(1)} - \sigma_{ow} L_{fow}^{(1)}. \quad (37) \end{aligned}$$

Again, $L_{sow}^{(1)} = L_{sgw}^{(1)}$ since the invading gas-water AM hinges at position $b_{gw}^{(1)} = b_{pd}$. The entry pressure $P_{cgw}^{N \rightarrow I}$ is calculated numerically as described above.

For bulk displacement E to I there does not exist any associated layer displacement. In this case the energy balance reduces to

$$\begin{aligned} \frac{\sigma_{gw}}{r_{gw}} (A_{gw}^{(1)} - A_{ow}^{(1)} + A_{ow}^{(2)}) + \frac{\sigma_{go}}{r_{go}} (A_{ow}^{(1)} - A_{ow}^{(2)}) = \\ \sigma_{gw} \cos \theta_{gwr} L_{sow}^{(2)} + \sigma_{go} \cos \theta_{gor} (L_{sgw}^{(1)} - L_{sow}^{(2)}) + \\ \sigma_{gw} L_{fgw}^{(1)} - \sigma_{ow} (L_{fow}^{(1)} - L_{fow}^{(2)}), \quad (38) \end{aligned}$$

where $L_{sow}^{(1)} = L_{sgw}^{(1)}$. The invading gas-water AM hinges with contact angle $\theta_{gwh}^{(1)}$ at position $b_{gw}^{(1)} = b_{pd}$, and thus the entry pressure $P_{cgw}^{E \rightarrow I}$ must be calculated by iterations.⁷

Having analyzed all the possible displacements for the specific combination of contact angles, we must formulate conditions for which each of the different scenarios can occur. The displacement from E to O can only occur if the entry pressures for the displacements E to N and E to I are less favourable. Additionally, we must require that the displacements resulting

from gas invasion into configuration O also are less favourable. More precisely, the displacement E to O can only occur if the entry pressures satisfy

$$P_{cij}^{E \rightarrow O} = \min\{P_{cij}^{E \rightarrow O}, P_{cij}^{O \rightarrow N}, P_{cij}^{O \rightarrow I}, P_{cij}^{E \rightarrow N}, P_{cij}^{E \rightarrow I}\}. \quad (39)$$

The displacement from configuration E to N occurs if Eq. 39 is not satisfied and the entry pressures satisfy

$$P_{cij}^{E \rightarrow N} = \min\{P_{cij}^{E \rightarrow N}, P_{cij}^{N \rightarrow I}, P_{cij}^{E \rightarrow I}\}. \quad (40)$$

If $P_{cij}^{E \rightarrow N}$ does not satisfy Eq. 40, then the displacement from E to I occurs.

The entry pressures for gas invasion into configuration O are only required to determine if the displacement E to O can occur. These layer displacements may occur at a more favourable entry pressure than the displacements from E to N, I or O. However, in cases where the displacement E to O does not occur, these entry pressures are superfluous and irrelevant, since the other bulk displacements are restricted by layer displacements involving other configurations. This is demonstrated by the condition for the displacement E to N given by Eq. 40, where the associated layer displacement is from configuration N to I.

$\theta_{gwr} < \pi/2 - \alpha$ and $\theta_{gor} \geq \pi/2 - \alpha$. For this combination of the contact angles, configuration N is not geometrically possible, since θ_{gor} does not satisfy Eq. 18. Gas invasion into configuration E results in either configuration I or O. The displacement from O to I is the only restricting layer displacement for the formation of configuration O in this case. Thus, the bulk displacement E to O can only occur if $P_{cij}^{E \rightarrow O}$ satisfies

$$P_{cij}^{E \rightarrow O} = \min\{P_{cij}^{E \rightarrow O}, P_{cij}^{O \rightarrow I}, P_{cij}^{E \rightarrow I}\}. \quad (41)$$

If Eq. 41 is not satisfied, the displacement from configuration E to I occurs instead.

$\pi/2 - \alpha \leq \theta_{gwr} \leq \pi/2 + \alpha$ and $\theta_{gor} < \pi/2 - \alpha$. For this set of contact angles, configuration O is not geometrically possible, since θ_{gwr} does not satisfy Eq. 18. Thus, gas into configuration E can only result in configuration N or I. The actual displacement occurring is from configuration E to N if the entry pressure $P_{cij}^{E \rightarrow N}$ satisfies

$$P_{cij}^{E \rightarrow N} = \min\{P_{cij}^{E \rightarrow N}, P_{cij}^{N \rightarrow I}, P_{cij}^{E \rightarrow I}\}. \quad (42)$$

If Eq. 42 is not satisfied, the displacement from configuration E to I occurs instead.

$\pi/2 - \alpha \leq \theta_{gwr} \leq \pi/2 + \alpha$ and $\theta_{gor} \geq \pi/2 - \alpha$. In this case θ_{gor} and θ_{gwr} do not satisfy Eq. 18, and thus layer formation is not possible. Gas into configuration E is always a displacement to configuration I.

$\theta_{gwr} > \pi/2 + \alpha$ and $\theta_{gor} < \pi/2 - \alpha$. For this combination of contact angles, gas invasion into configuration E may result in the layer displacements from E to P or J, and the bulk displacements from E to N or I. For the displacement E to P, the energy balance, given by Eqs. 26, 27, applies with $N_{go}^{fin} = N_{gw}^{fin} = N_{ow}^{fin} = 1$ for the resulting configuration P. This

yields

$$\begin{aligned} & \frac{\sigma_{gw}}{r_{gw}}(A_{ow}^{(2)} - A_{gw}^{(1)}) + \frac{\sigma_{go}}{r_{go}}(A_{go}^{(1)} - A_{ow}^{(2)}) = \\ & \sigma_{gw} \cos \theta_{gwr}(L_{sow}^{(2)} - L_{sgw}^{(1)}) + \sigma_{gw} L_{fgw}^{(1)} + \dots \quad (43) \\ & \sigma_{go} \cos \theta_{gor}(L_{sgo}^{(1)} - L_{sow}^{(2)}) + \sigma_{go} L_{fgo}^{(1)} - \sigma_{ow} L_{fow}^{(2)}. \end{aligned}$$

This equation may be formulated as a polynomial equation using Eqs. 20–25. Eventually, Eq. 32 is obtained and solved for r_{go} , and the corresponding entry pressure $P_{cgo}^{E \rightarrow P}$ is calculated from Eq. 11. The correct solution $P_{cgo}^{E \rightarrow P}$ must satisfy several restrictions. First, the entry pressure must be favourable compared to the collapse capillary pressure of the invading gas layer. Second, the invading gas-oil AM must invade at a position somewhere between the apex of the corner and the position $b_{ow}^{(2)}$ where the oil-water AM was located before the displacement. At last, the gas-water AM must invade at a position $b_{gw}^{(1)} > b_{ow}^{(2)}$. These conditions may be formulated as

$$\frac{\sigma_{go} \sin \beta_{gor}}{b_{ow}^{(2)} \sin \alpha} < P_{cgo}^{E \rightarrow P} < P_{go}^{col}, \dots \quad (44a)$$

$$\frac{\sigma_{gw} \sin \beta_{gwr}}{b_{ow}^{(2)} \sin \alpha} < P_{cgw}^{E \rightarrow P}. \dots \quad (44b)$$

where $P_{cgw}^{E \rightarrow P} = P_{cgo}^{E \rightarrow P} + P_{ow}$, and

$$P_{go}^{col} = \begin{cases} \frac{P_{ow} \frac{\sigma_{go} \cos \theta_{gor} - \sin \alpha}{\sigma_{gw} \cos \theta_{gwr} + \sin \alpha}}{1 - \frac{\sigma_{go} \cos \theta_{gor} - \sin \alpha}{\sigma_{gw} \cos \theta_{gwr} + \sin \alpha}} & \text{if } \theta_{gor} > \pi - \theta_{gwr}, \\ \frac{P_{ow} \frac{\sigma_{go} \cos(\theta_{gor} + \alpha)}{\sigma_{gw} \cos(\theta_{gwr} - \alpha)}}{1 - \frac{\sigma_{go} \cos(\theta_{gor} + \alpha)}{\sigma_{gw} \cos(\theta_{gwr} - \alpha)}} & \text{if } \theta_{gor} \leq \pi - \theta_{gwr}. \end{cases} \quad (45)$$

In cases where contact-angle hysteresis is absent, we only require $P_{cgo}^{E \rightarrow P} < P_{go}^{col}$.

If $P_{cgo}^{E \rightarrow P}$ only satisfies Eq. 44a, we calculate a new entry pressure for this displacement, assuming that the gas-water AM hinges with contact angle $\theta_{gwh}^{(1)}$ at position $b_{gw}^{(1)} = b_{ow}^{(2)}$. In this case Eq. 43 is employed with $L_{sgw}^{(1)} = L_{sow}^{(2)}$, and the entry pressure is calculated by an iterative procedure: For an initial value of r_{go} , e.g., $r_{go} = R$, we calculate r_{gw} from Eq. 13, and $\beta_{gwh}^{(2)}$ from 24 with $b_{gw}^{(1)} = b_{ow}^{(2)}$. Then the gas-water parameters $A_{gw}^{(1)}$ and $L_{fgo}^{(1)}$ are obtained from Eqs. 20–22. The gas-oil parameters $A_{go}^{(1)}$, $L_{fgo}^{(1)}$, $L_{sgo}^{(1)}$ are from Eqs. 20–23 with $\theta_{go}^{(1)} = \theta_{gor}$. An updated value of r_{go} is then calculated from the energy balance, Eq. 43. The procedure is repeated until convergence, and the entry pressure $P_{cgo}^{E \rightarrow P}$ is finally obtained from Eq. 11.

If $P_{cgo}^{E \rightarrow P}$ obtained from Eq. 32 only satisfies Eq. 44b, a new entry pressure is calculated from Eq. 43 assuming that the invading gas-oil AM hinges with contact angle $\theta_{goh}^{(1)}$ at position $b_{go}^{(1)} = b_{ow}^{(2)}$. In this case the gas-water AM is free to move.

Thus, Eq. 43 applies with $L_{sgo}^{(1)} = L_{sow}^{(2)}$. The entry pressure is calculated iteratively. For an initial value r_{go} , we obtain r_{gw} from Eq. 13. The gas-water parameters $A_{gw}^{(1)}$, $L_{fgo}^{(1)}$, $L_{sgw}^{(1)}$ are then calculated from Eqs. 20–23 with $\theta_{gw}^{(1)} = \theta_{gwr}$. Assuming that the gas-oil AM enters position $b_{go}^{(1)} = b_{ow}^{(2)}$, we obtain $\beta_{goh}^{(1)}$ from Eq. 24. The gas-oil parameters $A_{go}^{(1)}$ and $L_{fgo}^{(1)}$ are subsequently calculated from Eqs. 20–22. Finally, a new value of r_{go} is estimated from the energy balance, Eq. 43. This procedure is repeated until convergence, and the entry pressure is obtained from Eq. 11.

To decide if the displacement from configuration E to P is possible, we must also calculate the entry pressures for the related displacements resulting from gas invasion into configuration P, and examine if these displacements occur at less favourable entry pressures. This includes the bulk displacement P to N and the layer displacement P to J. The entry pressure $P_{cgw}^{P \rightarrow N}$ is calculated from Eqs. 26, 27 with $N_{ow}^{init} = N_{go}^{init} = N_{gw}^{init} = 1$ for configuration P, and with $N_{ow}^{fin} = N_{go}^{fin} = 1$, $N_{gw}^{fin} = 0$ for configuration N. This yields

$$\frac{A_{gw}^{(1)}}{r_{gw}} = L_{sgw}^{(1)} \cos \theta_{gwr} - L_{fgw}^{(1)}. \dots \quad (46)$$

If the gas-water AM in configuration P is free to move, an explicit expression for $P_{cgw}^{P \rightarrow N}$ can be derived.⁴ If the gas-water AM is hinging, the entry pressure is estimated numerically.⁴⁰ The layer displacement from P to J is similar to the displacement from N to E which we already have described.

Gas into configuration E may also result in a direct displacement to configuration J. In this case, Eqs. 26, 27 apply with $N_{ow}^{fin} = N_{go}^{fin} = 0$, $N_{gw}^{fin} = 2$ for configuration N. This yields

$$\begin{aligned} & \frac{\sigma_{gw}}{r_{gw}}(A_{gw}^{(1)} - A_{gw}^{(2)} - A_{ow}^{(1)} + A_{ow}^{(2)}) + \\ & \frac{\sigma_{go}}{r_{go}}(A_{ow}^{(1)} - A_{ow}^{(2)}) = \dots \quad (47) \\ & \sigma_{gw} \cos \theta_{gwr}(L_{sow}^{(2)} - L_{sgw}^{(2)}) + \sigma_{gw}(L_{fgw}^{(1)} + L_{fgw}^{(2)}) + \\ & \sigma_{go} \cos \theta_{gor}(L_{sgo}^{(1)} - L_{sow}^{(2)}) - \sigma_{ow}(L_{fow}^{(1)} + L_{fow}^{(2)}). \end{aligned}$$

The entry pressure is calculated numerically from Eq. 47, assuming that gw AM 1 hinges with contact angle $\theta_{gwh}^{(1)}$ at position $b_{gw}^{(1)} = b_{pd}$, whereas gw AM 2 is free to move with contact angle $\theta_{gwh}^{(2)} = \theta_{gwr}$. Starting with an initial value of r_{go} , e.g., $r_{go} = R$, we calculate r_{gw} from Eq. 11. Using Eq. 24 with $b_{gw}^{(1)} = b_{pd}$, we obtain a value for $\beta_{gwh}^{(1)}$ which is subsequently employed to calculate the parameters $A_{gw}^{(1)}$, $L_{fgo}^{(1)}$ from Eqs. 20–22. The parameters required for the second gas-water AM, $A_{gw}^{(2)}$, $L_{fgo}^{(2)}$, $L_{sgw}^{(2)}$, are estimated from Eqs. 20–23 with $\theta_{gw}^{(2)} = \theta_{gwr}$. An updated value for r_{go} is estimated from Eq. 47. The procedure is repeated until convergence, and the entry pressure $P_{cgo}^{E \rightarrow J}$ is finally obtained from Eq. 11. If contact-angle hysteresis is assumed and gw AM 2 invades at a position $b_{gw}^{(2)} < b_{ow}^{(2)}$, we solve Eq. 47 again assuming that *both* the gas-water

AMs enter the fixed positions $b_{ow}^{(1)} = b_{pd}$ and $b_{gw}^{(1)} = b_{ow}^{(2)}$ with hinging contact angles $\theta_{gwh}^{(1)}$ and $\theta_{gwh}^{(2)}$, respectively. In that case, the iterative procedure is slightly changed as both $\beta_{gwh}^{(1)}$ and $\beta_{gwh}^{(2)}$ are calculated from Eq. 24. These values are subsequently employed to estimate the gas-water parameters $A_{gw}^{(1)}$, $A_{gw}^{(2)}$, $L_{fgw}^{(1)}$, $L_{fgw}^{(2)}$ from Eqs. 20–22.

The layer displacement from configuration E to J is restricted by the bulk displacement J to I. This displacement is similar to the displacement P to N, and thus the corresponding entry pressure is calculated by Eq. 46.

The bulk displacements E to N and E to I may also occur for this combination of contact angles. These displacements, and related restricting displacements, have already been described.

To determine if a particular displacement occurs when gas enters configuration E, the entry pressure for this displacement must be favourable compared to the other possible displacements from configuration E. Additionally, if related displacements can originate when gas enters the resulting configuration, these must occur at less favourable entry pressures in order for the original displacement from configuration E to take place. The displacement from configuration E to P can only occur if

$$P_{cij}^{E \rightarrow P} = \min\{P_{cij}^{E \rightarrow P}, P_{cij}^{P \rightarrow N}, P_{cij}^{P \rightarrow J}, P_{cij}^{E \rightarrow J}, P_{cij}^{E \rightarrow N}, P_{cij}^{E \rightarrow I}\}. \quad (48)$$

The displacement E to J occurs if Eq. 48 is not satisfied, and $P_{cij}^{E \rightarrow J}$ satisfies

$$P_{cij}^{E \rightarrow J} = \min\{P_{cij}^{E \rightarrow J}, P_{cij}^{J \rightarrow I}, P_{cij}^{E \rightarrow N}, P_{cij}^{E \rightarrow I}\}. \quad (49)$$

The displacement from configuration E to N occurs if Eqs. 48, 49 are not satisfied while $P_{cij}^{E \rightarrow N}$ satisfies

$$P_{cij}^{E \rightarrow N} = \min\{P_{cij}^{E \rightarrow N}, P_{cij}^{N \rightarrow I}, P_{cij}^{E \rightarrow I}\}. \quad (50)$$

If Eqs. 48–50 are not satisfied, the displacement E to I occurs.

$\theta_{gr} > \pi/2 + \alpha$ and $\theta_{gor} \geq \pi/2 - \alpha$. For this combination of the contact angles only the layer displacement E to J and bulk displacement E to I are geometrically possible. Thus, the condition for which displacement E to J occurs, may be formulated as

$$P_{cij}^{E \rightarrow J} = \min\{P_{cij}^{E \rightarrow J}, P_{cij}^{J \rightarrow I}, P_{cij}^{E \rightarrow I}\}. \quad (51)$$

If Eq. 51 is not satisfied, the displacement E to I occurs.

Relationship Between the Entry Pressures and the Effect of Reversal Point

To investigate how bulk and layer displacements relate to each other, we calculate the corresponding entry pressures for various conditions. We first simulate primary drainage with $\theta_{pd} = 0^\circ$ to represent strongly water-wet conditions initially. The pore-wall surface in contact with oil experiences a wettability alteration. Waterflooding is simulated subsequently to establish configuration E. Then we study the entry pressures for the geometrically possible displacements that are allowed when gas invades configuration E. Two very different sets of interfacial tensions and contact angles are modelled to explore scenarios where different bulk and layer displacements can occur. The

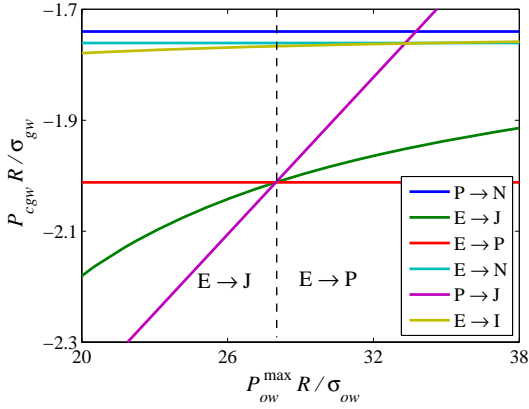
data are presented in **Table 1**. Case 1 represents a strongly oil-wet case where contact-angle hysteresis is absent. This may correspond to a condition where the pore walls are smooth ($\gamma = 0^\circ$). Case 2 represents a condition with a more realistic set of interfacial tensions and large contact-angle hysteresis ($\gamma = 50^\circ$). This may correspond to a condition where the pore walls have significant surface roughness. In this case the receding contact angles represent water-wet conditions, whereas the advancing contact angles represent strongly oil-wet conditions.

For gas invasion into configuration E, we present dimensionless gas-water capillary entry pressures for all possible displacements as functions of dimensionless oil-water capillary pressures. The pore size $R = 50 \mu\text{m}$ is considered in all examples. **Fig. 7(a)** shows the effect of P_{ow}^{\max} on the entry pressures for case 1. In this case $P_{ow} = -2.0$ kPa during gas invasion. An increased P_{ow}^{\max} corresponds to a decrease of water content in the corners of configuration E. Obviously, the entry pressures $P_{cgw}^{E \rightarrow N}$, $P_{cgw}^{E \rightarrow P}$ and $P_{cgw}^{P \rightarrow N}$ are independent of P_{ow}^{\max} as these displacements occur unaffected by the water in the corners. The entry pressures $P_{cgw}^{E \rightarrow J}$, $P_{cgw}^{E \rightarrow N}$ become increasingly affected by the water in the corners as P_{ow}^{\max} is decreased, whereas $P_{cgw}^{P \rightarrow J}$ seem to be strongly affected by the water in the corners for the entire range of P_{ow}^{\max} under consideration. As indicated in **Fig. 7(a)**, the actual displacement occurring is from E to J for small P_{ow}^{\max} . In this case, the displacement from P to J occurs at a lower entry pressure $P_{cgw}^{P \rightarrow J}$. However, this entry pressure becomes important only when configuration P already has formed, and this is not the case since the displacement E to P occurs at a higher entry pressure. Gas invasion into the new configuration J results in configuration I, which occurs at the entry pressure $P_{cgw}^{J \rightarrow I} = P_{cgw}^{P \rightarrow N}$. In this case, the entry pressures for the displacements E to P, E to I and E to N occurs at lower entry pressures. However, these entry pressures are irrelevant for the new configuration J as they are associated with configuration E.

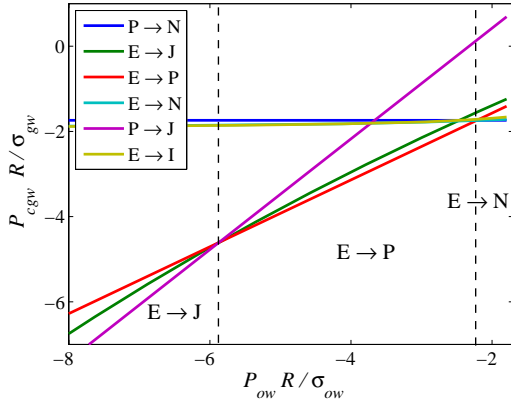
When P_{ow}^{\max} is increased, the displacement E to P becomes favourable. For moderate values of P_{ow}^{\max} the displacement sequence for gas invasion is from configuration E to P, from P to J and from J to I, while for higher P_{ow}^{\max} , the displacement sequence is from E to P, from P to N and from N to I. The point separating the different sequences appears in **Fig. 7(a)** where $P_{cgw}^{P \rightarrow J} = P_{cgw}^{P \rightarrow N}$. Again, the entry pressures for other displacements are more favourable, but these are irrelevant as the particular configurations involved have ceased to exist, or they have not yet been formed.

Fig. 7(b) shows the effect of oil-water capillary pressure on the gas-water entry pressure for case 1 with $P_{ow}^{\max} = 50$ kPa. **Fig. 7(c)** is a magnification of the upper right corner of **Fig. 7(b)**. In this case, the gas-water entry pressures for the layer displacements are more sensitive to P_{ow} than the bulk displacements. This is reasonable since the layer displacements mainly represent gas-oil displacements, while the bulk displacements mainly represent gas-water displacements. For small P_{ow} the displacement E to J occurs, for intermediate P_{ow} the displacement E to P occurs, and for large P_{ow} , the displacement E to N occurs.

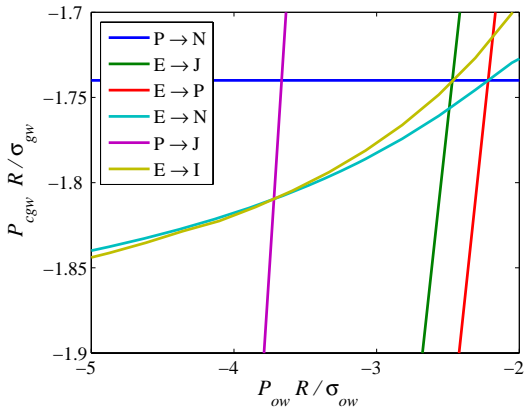
Fig. 7(b),(c) demonstrate how the different gas-water entry



(a)



(b)



(c)

Figure 7: Gas-water capillary entry pressures for gas into configuration E, case 1.

pressures are related to each other. Different combinations of three gas-water entry pressures coincide in four distinct points that separates different displacement sequences from each other. In the lower left corner, such a point occurs when $P_{cgw}^{E \rightarrow P} = P_{cgw}^{P \rightarrow J} = P_{cgw}^{E \rightarrow J}$. The occurrence of layer displacement E to P is restricted by layer displacement P to J. To the left of this separating point, the direct displacement E to J occurs, and to the right of the separation point, the displacement sequence E to P to J occurs. By tracking the $P_{cgw}^{P \rightarrow J}$ -curve a second point appears where $P_{cgw}^{E \rightarrow N} = P_{cgw}^{N \rightarrow I} = P_{cgw}^{E \rightarrow I}$ (notice that $P_{cgw}^{P \rightarrow J} = P_{cgw}^{N \rightarrow I}$). The bulk displacement from E to N is restricted by the layer displacement N to I. Therefore, the displacement sequence E to N to I is only possible to the right of the separation point, while the direct displacement E to I can only occur on the left side. Overall, neither of these displacements will occur since the displacement E to P occurs at a lower entry pressure. A third displacement separation point occurs where $P_{cgw}^{E \rightarrow I} = P_{cgw}^{E \rightarrow J} = P_{cgw}^{J \rightarrow I}$ (notice that $P_{cgw}^{J \rightarrow I} = P_{cgw}^{P \rightarrow N}$). The layer displacement E to J is restricted by bulk displacement J to I. Therefore, the displacement sequence E to J to I would only be possible to the left of this point. To the right, the direct displacement E to I would occur. Again, when all the entry pressures are considered as a whole, these displacements will not occur, as the displacement E to P still occurs at a more favourable entry pressure. The fourth point that separates different displacement sequences occurs when $P_{cgw}^{E \rightarrow P} = P_{cgw}^{P \rightarrow N} = P_{cgw}^{E \rightarrow N}$. In this case the actual displacement sequence occurring is from configuration E to P to N to the left, and from E to N to the right.

Recently, van Dijke *et al.*^{12,41} demonstrated that three-phase entry pressures in angular pores of uniform wettability without contact-angle hysteresis are consistent when both layer and bulk displacements are accounted for. This implies that for a unique combination of the capillary pressures, pores occupied by the same fluid in the bulk portion must have the same fluid configuration. The four distinct points that separate different displacement sequences from each other in **Fig. 7** indicate that three-phase entry pressures are also consistent in mixed-wet triangular pores even though layer and bulk displacements may occur while AMs in the corners hinge.

Fig. 8 demonstrates the effect of P_{ow} on the gas-water entry pressures for case 2 with $P_{ow}^{\max} = 100$ kPa. The two-phase displacement E to O is favourable for small P_{ow} , while the displacement E to N is favourable for large P_{ow} . The entry pressure $P_{cgw}^{N \rightarrow I}$ is not included in the figure since the displacement occurs at a much higher level of capillary pressure than the other displacements. This is due to the very high value of P_{ow}^{\max} used. The point separating the two displacement sequences occurs when $P_{cgw}^{E \rightarrow O} = P_{cgw}^{O \rightarrow N} = P_{cgw}^{E \rightarrow N}$. To the left of this point, the displacements occurring are from E to O to N to I, and to the right the displacement is directly from E to N, followed by the displacement N to I. The other point where three different entry pressures meet occurs when $P_{cgw}^{E \rightarrow O} = P_{cgw}^{O \rightarrow I} = P_{cgw}^{E \rightarrow I}$. To the left of this point, the displacements considered would be from configuration E to O to I, and to the right, directly from configuration E to I. This scenario would have been valid if gas-oil AMs did not form during the gas invasion. However, in this example, the displacement from configuration E to N is

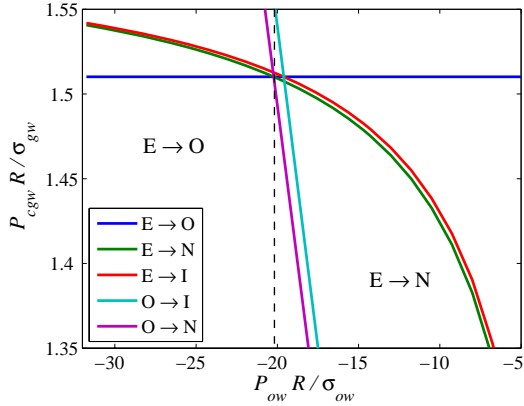


Figure 8: Three-phase entry pressures for gas into configuration E, case 2.

favourable compared to the displacement E to I for the entire range of P_{cow} where configuration E exists.

Since the contact angles of case 2 exhibit considerable hysteresis, we also investigate how the entry pressures relate when other displacement histories are established. We consider the sequence of processes primary drainage, imbibition, secondary drainage and gas invasion first. Primary drainage is terminated at $P_{ow}^{\max} = 100$ kPa, and imbibition is terminated at a capillary pressure P_{ow}^{\min} , where configuration E exists. Then secondary drainage is simulated until $P_{ow} = 0.10$ kPa, followed by gas invasion. At this capillary level, configuration E still exists while both the oil-water AMs hinge with a swelling oil layer in between. **Fig. 9** demonstrates the effect of P_{ow}^{\min} on the gas-water entry pressures for gas into configuration E. The amount of oil in layers increases according to P_{ow}^{\min} . This results in a sharp decrease of the entry pressures $P_{cgw}^{E \rightarrow N}$ and $P_{cgw}^{E \rightarrow I}$ for large P_{ow}^{\min} . The gas-water layer entry pressures depend strongly on P_{ow}^{\min} in the entire capillary pressure range where configuration E exists. The results presented in **Fig. 9** are analogous to those presented in **Fig. 8**. However, in the present example, the entry pressures for the displacements from configuration E to N and from O to N are calculated while the invading AMs are assumed to hinge. This is caused by the significantly higher pressure in the oil layers, as compared to the previous example in **Fig. 8** where the invading AMs in the same displacements were allowed to move. However, the entry pressures for these displacements still coincide with the entry pressure for the related displacement E to O in a single point. This indicates that the entry pressures calculated with hinging contact angles may also be consistent.

Finally, we consider an example of water invasion into configuration N for the parameters of case 2. In water invasion the entry pressures for the different displacements are calculated from the energy balance obtained by equating Eqs. 28, 29. The entry pressures for different combinations of the contact angles are derived in a similar fashion as for gas into configuration E. In the example considered here, the processes primary drainage, imbibition and gas invasion constitute the dis-

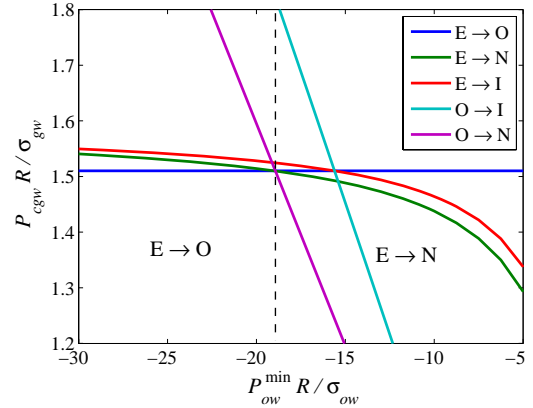


Figure 9: Three-phase entry pressures for gas into configuration E after secondary drainage, case 2.

placement history before the waterfloods are initiated. Primary drainage is terminated at $P_{ow}^{\max} = 50$ kPa, and imbibition is terminated at $P_{ow} = 2.0$ kPa. The effects of P_{go} on the gas-water entry pressures for the different bulk and layer displacements are presented in **Fig. 10**. For moderate values of P_{go} , the displacement from configuration N to E occurs, and for large P_{go} the displacement is from configuration N to P. The entry pressures for the displacements N to E and P to E are calculated assuming that the invading AMs hinge at fixed positions. For completeness, the corresponding entry pressures are also calculated assuming that the invading AMs are free to move with constant, advancing, contact angles. These entry pressures are indicated in **Fig. 10** by dashed lines of the same colour as the curves representing the actual entry pressures obtained with hinging AMs. The entry pressures $P_{cgw}^{N \rightarrow P}$, $P_{cgw}^{P \rightarrow D}$, $P_{cgw}^{N \rightarrow D}$ meet in a single point. Based on this restriction only, displacements occur directly from configuration N to D to the left of this separation point, and to the right, displacements occur from N to P to D. This scenario is true if gas-oil AMs can not form during water invasion, i.e., if the displacement N to E is impossible. However, as long as all the entry pressures are considered as a whole in the present example, the actual displacement occurring is from configuration N to E since the corresponding entry pressure is more favourable. The entry pressures for the displacements N to P, P to E and N to E coincide in a single point when $P_{cgw}^{N \rightarrow P} = P_{cgw}^{P \rightarrow E} = P_{cgw}^{N \rightarrow E}$. To the left of this point, the direct displacement N to E occurs, and to the right, the displacement N to P occurs. Subsequently, a displacement from P to E to D or directly from P to D occurs to the right, depending on where the layer entry pressures $P_{cgw}^{P \rightarrow E}$, $P_{cgw}^{E \rightarrow D}$, $P_{cgw}^{P \rightarrow D}$ meet. Even though it is not shown in the figure, it turns out that these layer entry pressures do not meet in a single point, and consequently they are not consistent. However, if we instead consider $P_{cgw}^{P \rightarrow E}$ calculated with AMs free to move (yellow dashed line), then the three entry pressures meet in a unique point, and consistency is obtained. However, with this value, the consistency is violated for the entry pressures $P_{cgw}^{N \rightarrow E}$, $P_{cgw}^{N \rightarrow P}$, $P_{cgw}^{P \rightarrow E}$.

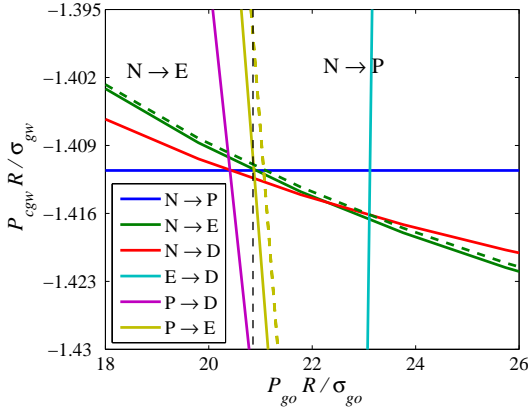


Figure 10: Three-phase entry pressures for water into configuration N, case 2.

If we also replace $P_{cgw}^{N \rightarrow E}$ by its equivalent calculated with moving AMs, the consistency is maintained also in this case. Notice that $P_{cgw}^{N \rightarrow P}$ coincides with the dashed yellow and green lines and also with the corresponding solid lines in two separate unique points. This may indicate that related entry pressures that completely account for hinging AMs are consistent. This is also true if the entry pressures are calculated while the AMs are free to move. However, by combining these two approaches, the entry pressures are generally not consistent, as demonstrated in **Fig. 10**. This is further emphasized by considering the point where $P_{cgw}^{N \rightarrow E}$, $P_{cgw}^{E \rightarrow D}$, $P_{cgw}^{N \rightarrow D}$ meet. In this case consistency is maintained if only the AMs present at position b_{pd} are allowed to hinge.

Relative Permeability and Saturation-Dependencies

With the present model, we calculate relative permeability vs. saturation relationships and study how variation of saturation reversal points in the displacement history affects the saturation-dependencies of three-phase relative permeabilities. The rel-perms are calculated by summing the conductances for each cross-sectional area that the fluid flows through, and dividing by the sum of conductances calculated as if the specific fluid flows through the entire pore space. This requires reliable expressions for the fluid conductances for layer, corner and bulk fluid areas. In this work we employ the expressions derived by Zhou *et al.*¹⁰ and Hui and Blunt.⁹ We assume no-slip conditions on the oil-water and fluid-solid boundaries, and perfect-slip conditions on the gas-oil and gas-water boundaries.

To demonstrate the sensitivity of saturation reversal points, we simulate primary drainage and wettability alteration, imbibition and gas invasion, where primary drainage is terminated at different P_{ow}^{\max} . To best illustrate our findings we consider the contact angles of case 3 where the advancing oil-water contact angle represents mild oil-wet conditions. In this case, the displacement C to D is likely to occur during the imbibition. Helland and Skjæveland⁴⁰ demonstrated that for this displacement the invasion order of the pore sizes is very sensitive to

P_{ow}^{\max} when $\theta_{owa} > \pi/2$. As a consequence, the bulk pore occupancies during imbibition also change according to P_{ow}^{\max} .⁷ For small P_{ow}^{\max} , water preferentially invades the small pore sizes first, and for large P_{ow}^{\max} , water preferentially invades the large pore sizes first. For intermediate P_{ow}^{\max} , water invasion may start in both the smaller and larger pores simultaneously. This may be explained as follows: The distance b_{pd} decreases as P_{ow}^{\max} is increased and thus the oil-wet area increases. Furthermore, the position b_{pd} is independent of pore size, and thus the water separated by the hinging AM in the corner affects the entry pressure in imbibition increasingly with decreasing pore size. This may result in non-monotonic invasion order of the pore sizes. We have previously demonstrated that the behaviour of the displacement types from C to D for different P_{ow}^{\max} results in different saturation-dependencies of three-phase capillary pressure in subsequent displacement processes.⁷ We will now explore if this is also the case for relative permeability.

A uniform distribution of pore sizes in the range from 1 μm to 50 μm , is assumed in the simulations. The rel-perms are calculated for both $P_{ow}^{\max} = 1.5$ kPa and $P_{ow}^{\max} = 15$ kPa. The displacement paths are shown in **Fig. 11(a), (b)**. In both cases gas displaces oil first, even though water is present in the small pores when $P_{ow}^{\max} = 1.5$ kPa and in large pores when $P_{ow}^{\max} = 15$ kPa. However, pronounced deviations are present in the calculated oil and gas iso-rel-perms in the two cases, as shown in **Fig. 11(c)–(f)**. When $P_{ow}^{\max} = 1.5$ kPa, gas invades subsequently smaller oil-filled pores, and hence gas occupies the large pores, while oil is present in the medium-sized pores. Such a pore occupancy occurs for water-wet conditions, and hence the oil rel-perm, k_{ro} , is a function of two saturations, while the gas and water rel-perms are functions of their own saturations.^{14,15} Furthermore, P_{ow} is a function of the water saturation, P_{go} is a function of the gas saturation, and P_{gw} depends strongly on two saturations.

When $P_{ow}^{\max} = 15$ kPa, gas starts to invade subsequently smaller oil-filled pores. However, in this case oil is located in the smaller pores, and hence gas occupies the medium-sized pores, while water is present in the large pore sizes. This scenario agrees well with typical pore occupancies for strongly oil-wet conditions, where gas behaves as the intermediate-wetting phase.^{14,15} In this case the gas phase is separated by gas-oil and gas-water boundaries, implying that the gas rel-perm, k_{rg} , is a function of two saturations, whereas the oil and water rel-perms are functions of their own saturations. The oil-water capillary pressure, P_{ow} , is still a function of the water saturation. However, the gas-oil capillary pressure, P_{go} , has now become a function of only the oil saturation, while P_{gw} is a function of only the water saturation.

These two examples illustrate that only by varying the amount of water in the corners of a mixed-wet pore, different saturation-dependencies of three-phase capillary pressure and relative permeability can occur. A similar sensitivity of saturation-reversal points may be achieved if secondary drainage is simulated before gas invasion. If configuration E exists at the end of imbibition, the reversal point P_{ow}^{\min} could have been varied instead to examine the effect of variable amounts of oil in layers, separated from bulk water by hinging AMs. This is similar to the

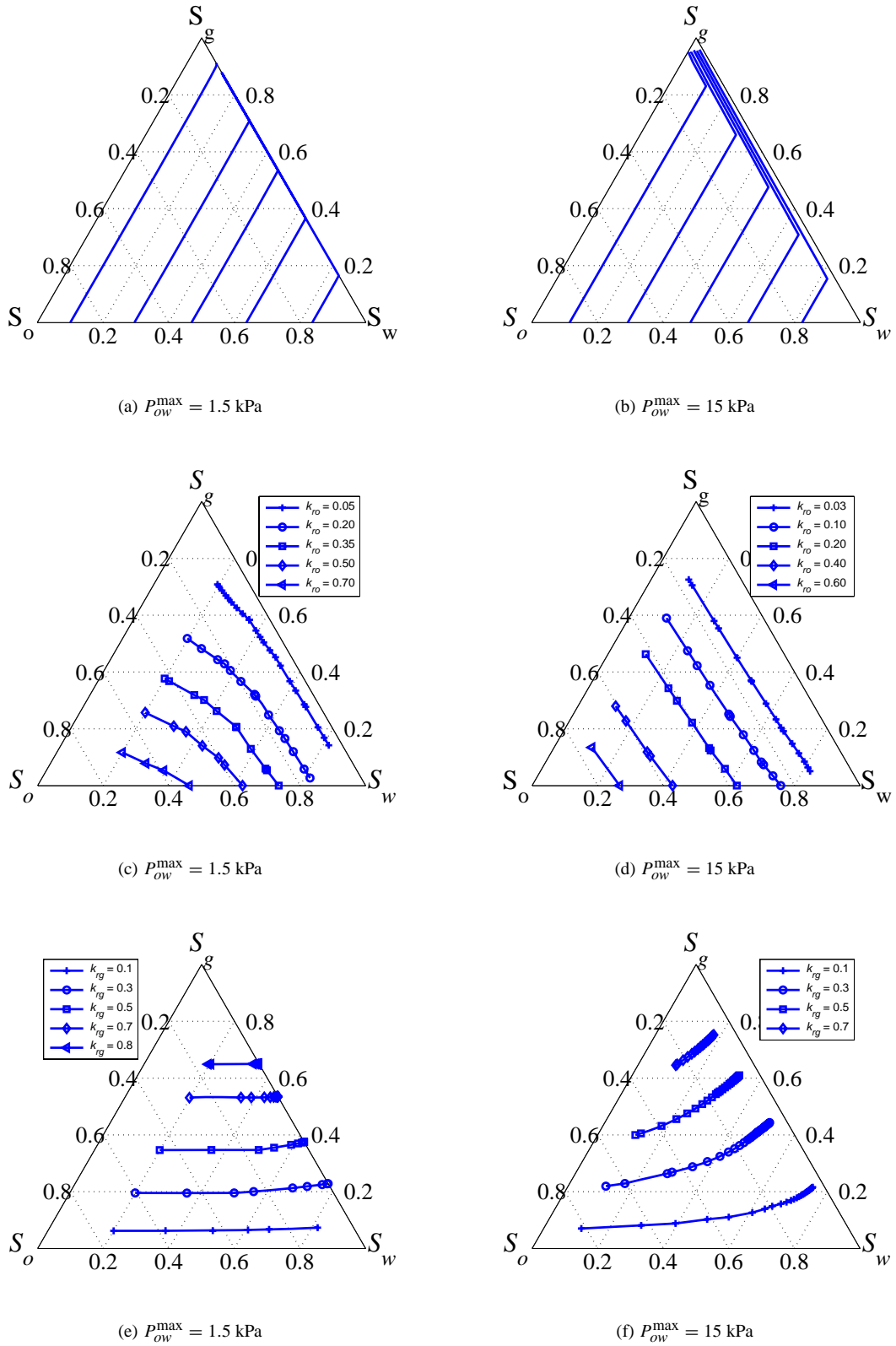


Figure 11: (a)–(b). Displacement paths. (c)–(d). Oil iso-rel-perms. (e)–(f). Gas iso-rel-perms

example studied in Fig. 9.

Conclusions

We have presented a model of mixed-wet triangular tubes that can be employed to calculate three-phase capillary pressure and relative permeability curves. Several fluid configurations may occur in triangular pore cross-sections, including configurations with one or more fluid layers present in the corners. We have derived accurate entry pressures for bulk and layer displacements using an energy balance that arises from minimization of Helmholtz free energy. To our knowledge, three-phase layer displacements in mixed-wet pores that also accounts for contact-angle hysteresis have not been analyzed before. We have described in detail how to deal with gas invasion into a configuration where oil layers separate water in the bulk and corners. We have also studied how the entry pressures for the different displacements relate to each other. Finally, the model was applied to calculate relative permeabilities which were analyzed with respect to their saturation-dependencies.

The conclusions are summarized as follows:

1. Our results indicate that three-phase entry pressures for mixed-wet conditions and contact-angle hysteresis are consistent if hinging and moving interfaces in the corners are treated consistently. We therefore hypothesize the following in order to maintain consistency between the related entry pressures:
 - If a displacement occurs with a hinging interface in the corner, then the entry pressure for any restricting displacement that involves the same interface must also be calculated assuming that the interface hinges.
 - If a displacement occurs with a moving interface in the corner, then the entry pressure for any restricting displacement that involves the same interface must also be calculated assuming that the interface moves.
2. Layer displacements may be very sensitive to saturation reversal points if contact-angle hysteresis or wettability alteration is assumed.
3. Three-phase relative permeability and capillary pressure and their saturation-dependencies may be very sensitive to saturation-reversal points in cases where interfaces hinge, i.e., when mixed-wet conditions are established, or when contact-angle hysteresis is assumed. In particular, variation of the maximum capillary pressure after primary drainage, P_{ow}^{\max} , may yield the following results:
 - For small P_{ow}^{\max} , the oil rel-perm depends on two saturations, while the gas rel-perm depends on the gas saturation.
 - For large P_{ow}^{\max} , the oil rel-perm depends on the oil saturation, while the gas rel-perm depends on two saturations.

The results from this work indicate that relative permeability and capillary pressure correlations should be formulated with parameters that strongly depend on saturation-reversal points such that different saturation-dependencies can be accounted for in subsequent invasion processes.

Acknowledgements

Support for Johan Olav Helland was provided by Statoil through the VISTA program.

References

1. Øren, P.E. and Pinczewski, W.V.: "Fluid distribution and pore-scale displacement mechanisms in drainage dominated three-phase flow," *Transport in Porous Media* (1995) **20**, 105–133.
2. Keller, A.A., Blunt, M.J., and Roberts, P.V.: "Micromodel observation of the role of oil layers in three-phase flow," *Transport in Porous Media* (1997) **26**, 277–297.
3. Mani, V. and Mohanty, K.K.: "Pore-level network modeling of three-phase capillary pressure and relative permeability curves," *SPEJ* (Sept. 1998) 238–248.
4. Øren, P.E., Bakke, S., and Arntzen, O.J.: "Extending predictive capabilities to network models," *SPEJ* (Dec. 1998) 324–336.
5. Blunt, M.J., Jackson, M.D., Piri, M., and Valvatne, P.H.: "Detailed physics, predictive capabilities and macroscopic consequences for pore-network models of multiphase flow," *Adv. Water Resources* (2002) **25**, 1069–1089.
6. Piri, M. and Blunt, M.J.: "Three-dimensional mixed-wet random pore-scale network modeling of two- and three-phase flow in porous media. I. Model description," *Phys. Rev. E* (2005) **71**, No. 026301.
7. Helland, J.O. and Skjæveland, S.M.: "Three-phase mixed-wet capillary pressure curves from a bundle-of-triangular-tubes model," paper presented at the 8th International Symposium on Reservoir Wettability, Houston, TX, May 16–18, 2004. Revised version accepted for publication in *J. Pet. Sci. Eng.*
8. Kovscek, A.R., Wong, H., and Radke, C.J.: "A pore-level scenario for the development of mixed wettability in oil reservoirs," *Am. Inst. Chem. Eng. J.* (1993) **39**, No. 6, 1072–1085.
9. Hui, M.H. and Blunt, M.J.: "Effects of wettability on three-phase flow in porous media," *J. Phys. Chem. B* (2000) **104**, 3833–3845.
10. Zhou, D., Blunt, M., and Orr, Jr., F.M.: "Hydrocarbon drainage along corners of noncircular capillaries," *J. Coll. Int. Sci.* (1997) **187**, 11–21.
11. van Dijke, M.I.J. and Sorbie, K.S.: "Three-phase capillary entry conditions in pores of noncircular cross-section," *J. Coll. Int. Sci.* (2003) **260**, 385–397.
12. van Dijke, M.I.J., Lago, M., Sorbie, K.S., and Araujo, M.: "Free energy balance for three fluid phases in a capillary of arbitrarily shaped cross-section: capillary entry pressures and layers of the intermediate-wetting phase," *J. Coll. Int. Sci.* (2004) **277**, 184–201.
13. Jadhunandan, P.P. and Morrow, N.R.: "Effect of wettability on waterflood recovery for crude-oil/brine/rock systems," *SPEJ* (Feb. 1995) 40–46.
14. van Dijke, M.I.J., McDougall, S.R., and Sorbie, K.S.: "Three-phase capillary pressure and relative permeability relationships in mixed-wet systems," *Transport in Porous Media* (2001) **44**, 1–32.
15. van Dijke, M.I.J., Sorbie, K.S., and McDougall, S.R.: "Saturation-dependencies of three-phase relative permeabilities

- in mixed-wet and fractionally-wet systems," *Adv. Water Resources*. (2001) **24**, 365–384.
16. Bradford, S.A. and Leij, F.J.: "Fractional wettability effects on two- and three-fluid capillary pressure-saturation relations," *J. Cont. Hydr.* (1995) **20**, 89–109.
 17. Bradford, S.A. and Leij, F.J.: "Wettability effects on scaling two- and three-fluid capillary pressure-saturation relations," *Env. Sci. Tech.* (1995) **29**, 1446–1455.
 18. Bradford, S.A. and Leij, F.J.: "Predicting two- and three-fluid capillary pressure-saturation relationships of porous media with fractional wettability," *Water Resources Research* (1996) **32**, No. 2, 251–259.
 19. Ma, S., Mason, G., and Morrow, N.R.: "Effect of contact angle on drainage and imbibition in regular polygonal tubes," *Coll. Surf. A: Phys. Eng. Asp.* (1996) **117**, 273–291.
 20. Hiemenz, P.C. and Rajagopalan, R.: *Principles of colloid and surface chemistry*, 3rd edition, Marcel Dekker, New York (1997).
 21. Zhou, D. and Blunt, M.J.: "Effect of spreading coefficient on the distribution of light non-aqueous phase liquid in the subsurface," *J. Cont. Hydr.* (1997) **25**, 1–19.
 22. van Dijke, M.I.J. and Sorbie, K. S.: "The relation between interfacial tensions and wettability in three-phase systems: Consequences for pore occupancy and relative permeability," *J. Pet. Sci. Eng.* (2002) **33**, 39–48.
 23. van Dijke, M.I.J. and Sorbie, K.S.: "Cusp at the three-fluid contact line in a cylindrical pore," *J. Coll. Int. Sci.* (2005) Article in press.
 24. Long, J., Hyder, M.N., Huang, R.Y.M., and Chen, P.: "Thermodynamic modeling of contact angles on rough heterogeneous surfaces," *Adv. Int. Sci.* (2005) **118**, 173–190.
 25. Morrow, N.R.: "The effects of surface roughness on contact angle with special reference to petroleum recovery," *J. Can. Pet. Tech.* (1975) **14**, No. 4, 42–53.
 26. Paterson, A., Robin, M., Fermigier, M., Jenffer, P., and Hulin, J.P.: "Effect of density and spatial distribution of wettability heterogeneities on contact angle," *J. Pet. Sci. Eng.* (1998) **20**, 127–132.
 27. Yang, S.-Y., Hirasaki, G.J., Basu, S., and Vaidya, R.: "Mechanisms for contact angle hysteresis and advancing contact angles," *J. Pet. Sci. Eng.* (1999) **24**, 63–73.
 28. Xie, X., Morrow, N.R., and Buckley, J.S.: "Contact angle hysteresis and the stability of wetting changes induced by adsorption from crude oil," *J. Pet. Sci. Eng.* (2002) **33**, 147–159.
 29. Kumar, K., Dao, E., and Mohanty, K.K.: "AFM study of mineral wettability with reservoir oils," *J. Coll. Int. Sci.* (2005) **289**, 206–217.
 30. Mayer, R.P. and Stowe, R.A.: "Mercury porosimetry – breakthrough pressure for penetration between packed spheres," *J. Coll. Sci.* (1965) **20**, 893–911.
 31. Princen, H.M.: "Capillary phenomena in assemblies of parallel cylinders. I. Capillary rise between two cylinders," *J. Coll. Int. Sci.* (May 1969) **30**, No. 1, 69–75.
 32. Princen, H.M.: "Capillary phenomena in assemblies of parallel cylinders. II. Capillary rise in systems with more than two cylinders," *J. Coll. Int. Sci.* (Jul. 1969) **30**, No. 3, 359–371.
 33. Princen, H.M.: "Capillary phenomena in assemblies of parallel cylinders. III. Liquid columns between horizontal parallel cylinders," *J. Coll. Int. Sci.* (Oct. 1970) **34**, No. 2, 171–184.
 34. Mason, G. and Morrow, N.R.: "Capillary behavior of a perfectly wetting liquid in irregular triangular tubes," *J. Coll. Int. Sci.* (1991) **141**, 262–274.
 35. Lago, M. and Araujo, M.: "Threshold pressure in capillaries with polygonal cross section," *J. Coll. Int. Sci.* (2001) **243**, 219–226.
 36. Piri, M. and Blunt, M.J.: "Pore-scale modeling of three-phase flow in mixed-wet systems," paper SPE 77726 presented at the 2002 SPE Annual Technical Conference and Exhibition, San Antonio, TX, Sept. 29–Oct. 2.
 37. Piri, M. and Blunt, M.J.: "Three-phase threshold capillary pressures in non-circular capillary tubes with different wettabilities including contact angle hysteresis," *Phys. Rev. E* (2004) **70**, No. 061603.
 38. Fenwick, D.H. and Blunt, M.J.: "Three-dimensional modeling of three phase imbibition and drainage," *Adv. Water Resources* (1998) **25**, No. 2, 121–143.
 39. Firincioglu, T., Blunt, M.J., and Zhou, D.: "Three-phase flow and wettability effects in triangular capillaries," *Coll. Surf. A: Phys. Eng. Asp.* (1999) **155**, 259–276.
 40. Helland, J.O. and Skjæveland, S.M.: "Physically-based capillary pressure correlation for mixed-wet reservoirs from a bundle-of-tubes model," paper SPE 89428 presented at the 2004 SPE/DOE Fourteenth Symposium on Improved Oil Recovery, Tulsa, OK, Apr. 17–21.
 41. van Dijke, M.I.J. and Sorbie, K.S.: "Consistency of three-phase capillary entry pressures and pore phase occupancies," paper submitted to *Adv. Water Resources* (2005).

Case	σ_{gw} (N/m)	σ_{ow} (N/m)	σ_{go} (N/m)	γ (°)	θ_{owe} (°)	θ_{gwe} (°)	θ_{goe} (°)	θ_{owa} (°)	θ_{owr} (°)	θ_{gwa} (°)	θ_{gwr} (°)	θ_{goa} (°)	θ_{gor} (°)
1	0.030	0.039	0.010	0	180	165.2	0	180	180	165.2	165.2	0	0
2	0.030	0.020	0.012	50	120	87.1	16.6	170	70	137.1	37.1	66.6	0
3	0.030	0.020	0.012	30	100	73.5	0	130	70	103.5	43.5	30	0

Table 1: Interfacial tensions and contact angles used in the simulations.